Universidad
Carlos III de Madrid

Final Year Project in Industrial Engineering, specialized in Materials science and engineering.

"Development and optimization of an AA2014 powder metallurgy aluminium alloy, characterization and corrosion behavior"

Author: Enrique Redondo Ruiz

Tutor: Diógenes Carbonell Boix

ACKNOWLEDGMENTS

First, I would like to express my profound gratitude and deep regards to my tutor, Diógenes Carbonell, for his dedications and the many things he has taught me, as well as offering me the opportunity to work with him. For that, I also want to thank Mónica Campos and Antonia Jiménez.

I want to give a special mention to Departamento de Ciencia de Materiales e Ingeniería Química de la Universidad Carlos III de Madrid, especially the Grupo de Tecnología de Polvos. They have been extremely helpful at all times and have make working there a great experience. Special mention to Amaya García, Elena Bernardo, Roberto García, Javier Hidalgo, Raquel de Oro, Paula Alvaredo and many others.

Finally, I would like to thank my family and friends for all the support received during these years.

Contents

Figure index

Table index

ABSTRACT AND AIM

The light density of aluminium has make it one of the main materials used in the aeronautic and automotive industries. Both industries are constantly trying to reduce weight to save costs in combustibles. When heat treated, aluminium alloys obtain values of specific strength that allows them to compete with ferrous alloys.

Powder metallurgy is an alternative to conventional manufacturing techniques, such as casting or forging. It can produce small pieces at high rate with a high complexity, requiring much less machining process, thus saving time, costs and raw material.

The aim of this project is the characterization and optimization of an aluminium alloy, AA2014 T4, manufactured by powder metallurgy.

The experimental procedures focused on the manufacture of samples of the alloy, following a conventional powder metallurgy route of press-and-sinter and optimizing the parameter of compaction pressure. A series of tests were carried out to evaluate the sample's physical and mechanical properties, its microstructure and its corrosion resistance.

This project includes:

1. A characterization of the starting powders, studying the distribution of particle sizes and the morphology of the powders.

2. Mixing of the powders with a lubricant, uniaxial compaction and characterization of the green part, measuring density, porosity and flexural strength.

3. Theoretical study of the sintering temperature, analyzing the phase diagram of the alloy and supporting the decision with a thermogravimetric analysis.

4. Sintering, heat treatment and characterization of the final product: density, porosity, flexural strength, hardness, microstructure (through X-rays crystallography and scanning electron microscope) and corrosion resistance (through electrochemical impedance spectroscopy).

Keywords: Aluminium Alloys, AA2014, Powder Metallurgy, Sintering, EIS

RESUMEN Y OBJETIVOS

La baja densidad del aluminio le ha convertido en uno de los materiales más usados en las industrias de aeronáutica y automoción. Ambas industrias buscan sin descanso reducir el peso de los vehículos para ahorrar costes en consumo de combustible. Después de un tratamiento térmico, las aleaciones de aluminio pueden alcanzar valores de resistencia específica que les permiten competir con aleaciones férreas.

La metalurgia de polvos es una alternativa a las técnicas de fabricación convencionales, como moldeo o forja. Con ella, es posible producir piezas de pequeño tamaño con una gran complejidad, requiriendo menos mecanización, lo que ahorra tiempo, coste y material.

El objetivo de este proyecto es caracterizar y optimizar una aleación de aluminio, AA2014 T4, fabricada por metalurgia de polvos.

El procedimiento experimental se centró en fabricar muestras de la aleación, siguiendo una ruta convencional de metalurgia de polvos de *press-and-sinter*, y en optimizar el parámetro de presión de compactación. Se realizaron una serie de experimentos de cara a evaluar las propiedades físicas y mecánicas de las muestras, además de observar su microestructura y su resistencia a corrosión.

Este proyecto incluye:

1. Una caracterización de los polvos de partida, incluyendo distribución de tamaños de partícula y morfología de los polvos.

2. Mezclado de los polvos con un lubricante, compactación uniaxial y caracterización de la muestra en verde, midiendo densidad, porosidad y resistencia a flexión.

3. Estudio teórico de la temperatura de sinterizado, analizando el diagrama de fases de la aleación y realizando un análisis termogravimétrico para apoyar la decisión.

4. Sinterizado, tratamiento térmico y caracterizado del producto final: densidad, porosidad, Resistencia a flexión, dureza, microestructura (a través de difracción de rayos X y microscopía de barrido electrónica) y resistencia de corrosión (usando espectroscopia de impedancia electroquímica).

Palabras clave: Aleaciones de aluminio, AA2014, Metalurgia de Polvos, Sinterizado, EIS

CHAPTER 1: INTRODUCTION

1.1. Aluminium

Aluminium is one of the most consumed metal in the world, only second after Steel. It is also the third most abundant element in the Earth's crust with around 8% of it being aluminium. It is found in the mineral bauxite, in the form of aluminium oxide (Al_2O_3). Aluminium is obtained by reduction of its oxide using electrolysis.

Aluminium's main property, its low density (second lowest between metals, after magnesium), has made it an interesting compound for the aeronautical industry and other engineering applications. It is also heavily used in the distribution of electricity through the use of overhead cables, due to being a light-weight metal with high electrical conductivity. We can find aluminium being used in low weight structures, buildings, packaging, automotive, marine applications, aerospace and electrical applications, such as conductors or capacitors.

Aluminium density is 2.7 g/cm^3, around 3 times less than steel's 7.83 g/cm^3 and copper 8.93 g/cm^3. Because of this, its specific Young Modulus is the same as steel and its specific electrical conductivity is higher than copper's. Aluminium has a melting point is 660 ºC and high corrosion resistance [1-4].

1.2. Aluminium Alloys

Pure Aluminium has low strength, requiring to be alloyed with other elements to be usable in most applications. By adding other elements, we can increase tensile strength up to almost 700 MPa. This high strength combined with lower density than other metals results in a high specific strength, an important parameter for most structural applications. However, this comes at the cost of reducing Aluminium excellent corrosion resistance [5].

Aluminium Association (AA) divide Aluminiun alloys in casting compositions and wrought compositions (Figures 1.1 and 1.2). Casting alloys are those were the product is formed without any plastic deformation, whereas wrought alloys are formed through the use of deformation (hot or cold). Both types are classified in series to describe the composition of the material [6].

- 1*xx.x* Controlled unalloyed (pure) compositions, especially for rotor manufacture
- 2*xx.x* Alloys in which copper is the principal alloying element, but other alloying elements may be specified
- 3*xx.x* Alloys in which silicon is the principal alloying element, but other alloying elements such as copper and magnesium are specified
- 4*xx.x* Alloys in which silicon is the principal alloying element
- 5*xx.x* Alloys in which magnesium is the principal alloying element
- 6*xx.x* Unused
- 7*xx.x* Alloys in which zinc is the principal alloying element, but other alloying elements such as copper and magnesium may be specified
- 8*xx.x* Alloys in which tin is the principal alloying element
- 9*xx.x* Unused

Figure 1.1: Casting compositions [1].

- 1xxx Controlled unalloyed (pure) compositions
- 2xxx Alloys in which copper is the principal alloying element, though other elements, notably magnesium, may be specified
- 3xxx Alloys in which manganese is the principal alloying element
- 4xxx Alloys in which silicon is the principal alloying element
- 5xxx Alloys in which magnesium is the principal alloying element
- 6xxx Alloys in which magnesium and silicon are principal alloying elements
- 7xxx Alloys in which zinc is the principal alloying element, but other elements such as copper, magnesium, chromium, and zirconium may be specified
- 8xxx Alloys including tin and some lithium compositions characterizing miscellaneous compositions
- 9xxx Reserved for future use

Figure 1.2: Wrought compositions [1].

The alloy used in this project is AA2014, belonging to the 2xxx series. This series uses Copper as its main alloying element. Through heat treatment and aging treatments, its mechanical properties become higher than those of low-carbon steels. They are often used for designs that require high specific strength, such as aeronautical or automotive applications. Its corrosion resistance is worse than high-purity aluminium due to intergranular or pitting corrosion, as well as other less common types of corrosion [7].

AA2014 is typically used for aircraft fittings, wheels, and major structural components, space booster tankage and structure, truck frame and suspension components. In general, it is used for applications requiring high strength and hardness that include service at elevated temperatures [8].

1.3. Heat treatments

A temper designation is usually added after the series digits to indicate the mechanical and/or thermal treatments realized. The basic designations are: F (fabricated), O (annealed), H (strain-hardened), W (solution heat-treated for unstable tempers) and T (solution heat treated). Additional digits are used to provide additional details about the mechanic or heat treatment. Table 1.1 shows the designations for heat-treatments.

Table 1.1: Temper designations [6].

T1	Cooled from an elevated-temperature shaping process and naturally aged to substantially stable condition
T2	Cooled From an Elevated-Temperature Shaping Process, Cold Worked, and Naturally Aged to a Substantially Stable Condition
T3	Solution Heat Treated, Cold Worked, and Naturally Aged to a Substantially Stable Condition
T4	Solution Heat Treated and Naturally Aged to a Substantially Stable Condition
T5	Cooled From an Elevated-Temperature Shaping Process and Artificially Aged
T6	Solution Heat Treated and Artificially Aged
T7	Solution Heat Treated and Overaged or Stabilized
T8	Solution Heat Treated, Cold Worked, and Artificially Aged
T9	Solution Heat Treated, Artificially Aged, and Cold Worked
T10	Cooled From an Elevated-Temperature Shaping Process, Cold Worked, and Artificially Aged

Heat-treatment is possible with elements that increase their solubility at higher temperatures (Figure 1.3). That will lead to the formations of clusters of the solute, which, if they are coherent (i.e., having the same crystal structure) with aluminium, they will share the dislocation-containing interface with the matrix. The different sizes of the atoms will stabilize dislocations, which are trapped by coherent clusters and thus increase the alloy strength and hardness.

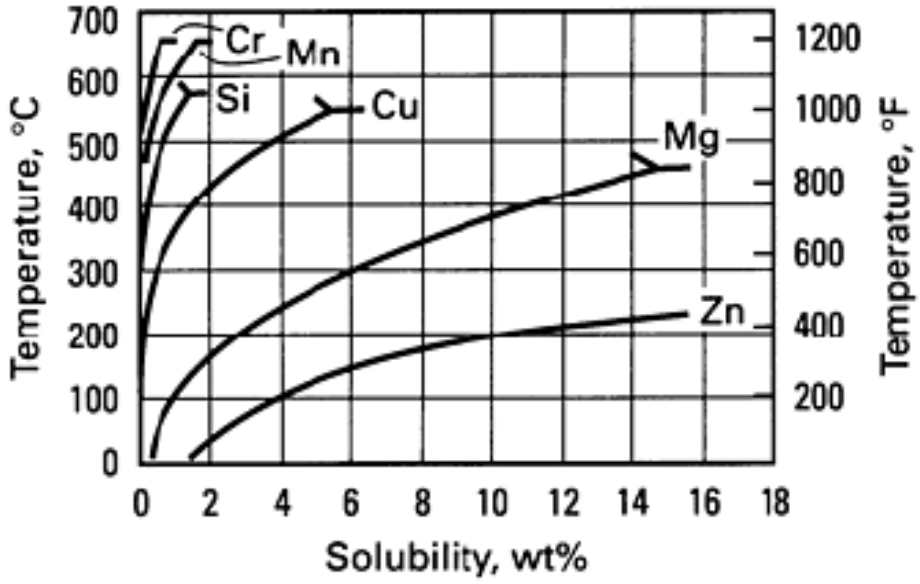

Figure 1.3: Solubility of different elements in aluminium [7].

The heat treatment consist in a "Solution Heat Treatment" at high temperature to solubilize the alloying elements in the matrix. For the case of copper in aluminiun, this requires temperatures over the solvus line, at around 500 ºC. After that, the alloy is cooled fast (quenching) to a low temperature. The result is a solid solution supersaturated with solute elements. By rapidly cooling we avoid the formation of a softer equilibrium structure.

During the aging treatment, finely dispersed precipitates are formed. First, solute atoms cluster to form Guinier-Preston (GP) zones, which are of two types: GP1 zones are formed first and then they grow into GP2 zones, responsible for the maximum strength (Figure 1.4). The presence of magnesium as alloying element increases and accelerates precipitation. The precipitation process can be performed at room temperature ("Natural aging") or at higher temperatures ("Artificial aging"). Artificial aging gains hardness and strength faster but forms softer equilibrium precipitates. It can also result in even softer precipitates due to overaging (see Figure 1.5) [9, 10].

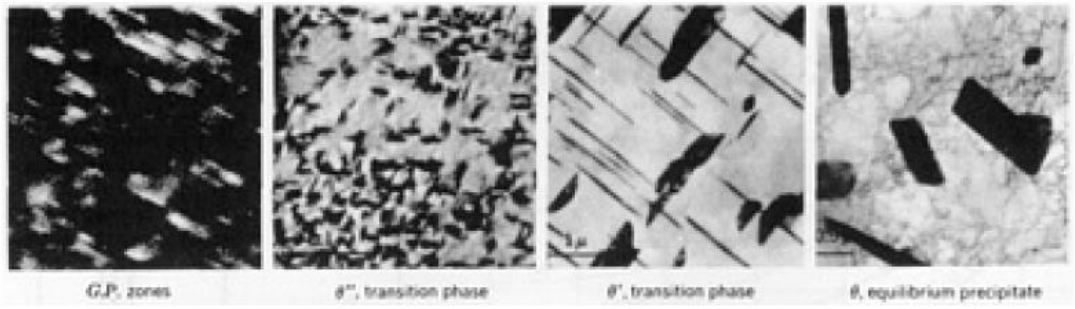

Figure 1.4: Images obtained by TEM of the different phases of the aging process [9].

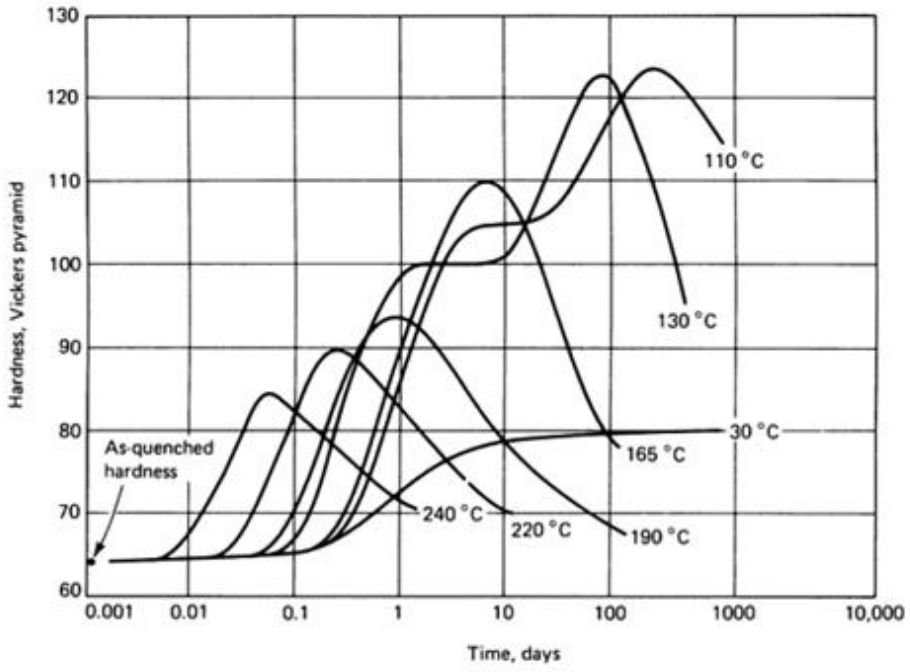

Figure 1.5: Hardness as a function of the aging temperature and time for an Al-4Cu alloy [9].

1.4. Powder metallurgy

Powder metallurgy (PM) is a technique that produces small, complex pieces at fast rates, with low waste of material and similar properties to other methods, such as casting. PM involves the production of powders, compression of it to form the part, sintering and finishing operations.

PM parts usually have lower density than the theoretical density, due to residual porosity. This influences heavily the final properties, lowering mechanical properties and electrical and thermal conductivities. Parts with lower properties can still be cost effective when compared to castings and forgings, due to requiring less machining and having high rates of production. In addition, PM also allows to produce any alloy system available as powders, being the only commercially viable method for some materials [11].

PM's large variety of processes can be divided into two groups: conventional press-and-sinter processes and full-density processes. The first group provide fair properties at an excellent cost, while full-density processes such as MIM or HIP provide high density and therefore, high

mechanical properties, although at higher costs. Table 1.2 provides a good summary of the advantages and disadvantages of each process [12].

Table 1.2: Comparison of different powder processing techniques [12].

Characteristic	Conventional	MIM	HIP	P/F
Size	Good	Fair	Excellent	Good
Shape complexity	Good	Excellent	Very good	Good
Density	Fair	Very good	Excellent	Excellent
Dimensional tolerance	Excellent	Good	Poor	Very good
Production rate	Excellent	Good	Poor	Excellent
Cost	Excellent	Good	Poor	Very good

1.4.1. Uniaxial die compaction

Pressure is applied with punches that move in the vertical direction while the powder is placed in rigid dies. To correctly apply pressure, there are limitations on the shape of the parts. Due to the non-uniform transmission of pressure through the mass of powder, compacted parts have different densities (Figure 1.6). To reduce density variation, multiple punches can be used for different thickness or applying pressure from the top and the bottom. Lubricants help by reducing the friction between the die wall and the powder. They are either mixed with the powder or applied to the walls. Due to friction with walls, tall and thin parts would have high density variance [13].

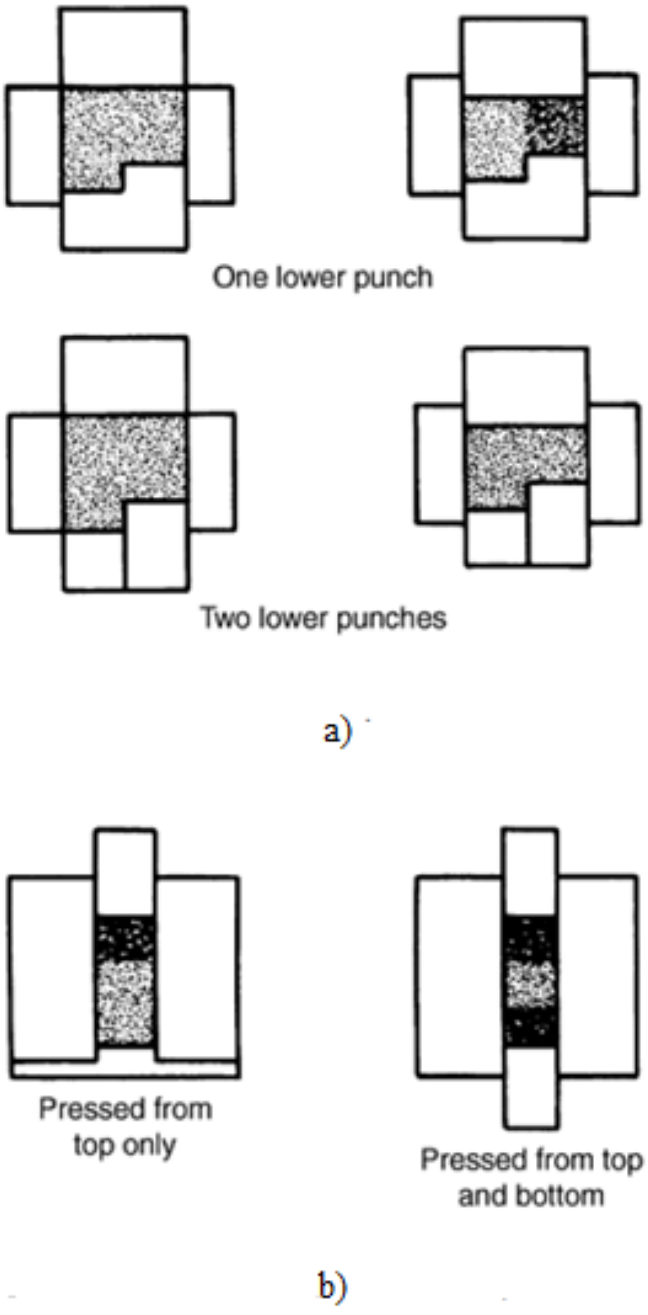

Figure 1.6: a) Density distribution for multiple-levels compacts. b) Density distribution for compacts [13].

Powder is poured into a die and a movable punch seals the opening and applies pressure (see Figure 1.7). For simple parts, one moving punch may be enough. More complex parts require additional punches to reduce density gradients [14].

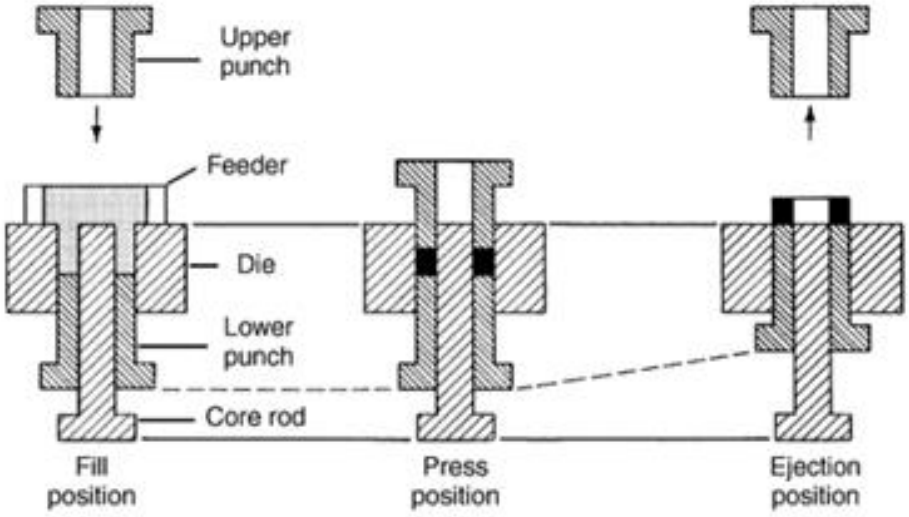

Figure 1.7: Compacting sequence [14].

The press used can be mechanical or hydraulic. A mechanical press has higher production rates compared to a hydraulic press, as well as better energy efficiency, thus having lower operating costs. However, the equipment cost for a hydraulic press is lower than for a mechanical press. Hydraulic presses can compact at higher pressures than mechanical presses.

Green density usually ranges between 75 and 85% of the theoretical density. It is increased with the load applied. It is also affected by factors like powder shape, particle size and distribution, type of powder (prealloyed, master alloy, etc.) or lubrication. Compacting pressures for aluminium powders range from 100 MPa to 400 MPa.

1.4.2. Sintering

Sintering is a heat treatment at temperatures below the melting point of the main constituent in which compact particles form chemical bonds, resulting in a coherent material. Sintering involves a series of material transport mechanisms that produce densification and consolidation. Densification increases most mechanical properties. However, it also causes dimensional changes and shrinkage, reducing tolerances.

The principal driving force for the material transport is the reduction in surface energy, related to the curvature of the surfaces and interfaces. This causes the necks between particles to grow during the first stages of sintering. During the following stages, the pores between particles acquire a rounded shape and the channels between pores close. In the last stages, the pores shrinks, causing densification.

The material transport mechanisms can be different types of diffusion (surface, volume or grain boundary), viscous flow or evaporation and condensation (see Figure 1.8). Sintering can be done with or without the formation of liquid. Liquid-phase sintering has the advantage of an easier diffusion and reaching higher densities at lower temperatures. However, dimensional control is better in solid-state sintering [15, 16].

Cycle time and temperature are the most important parameters of sintering. For aluminium alloys, temperatures are around 600 ºC, with sintering times typically between 20 and 60 min [17].

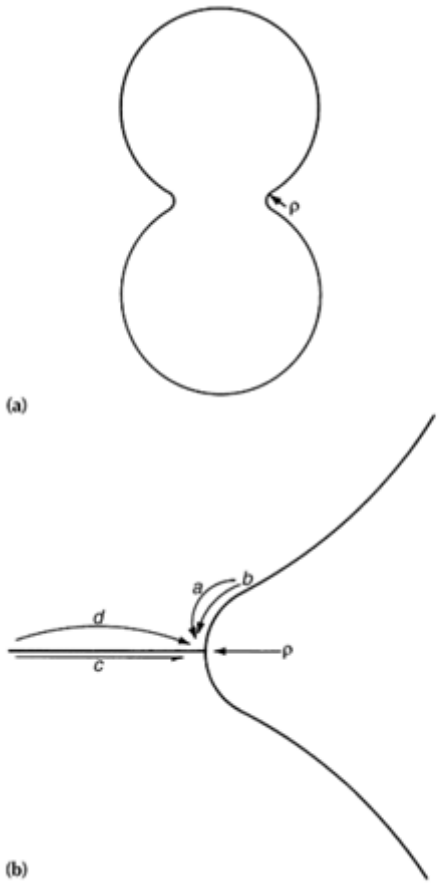

Figure 1.8: Sintering mechanisms; a) Two spheres sintering together. b) Types of matterial transport: a - volume diffusion from the flat surface to the neck; b - surface diffusion from the flat surface to the neck; c - grain-boundary diffusion from the grain boundary to the neck; d - volume diffusion from the grain boundary to the neck [15].

The atmosphere performs different functions during sintering. The most important one is the protection of the heated material from the effects of air, especially oxygen. Additionally, the atmosphere also needs to ensure a uniform heat transfer. For aluminium, sintering is usually done in nitrogen at high purity and low dew point. Nitrogen is obtained from air. It is inert and has a density similar to air's, thus preventing it from entering the furnace. Dissociated ammonia can also be used, though the resulting tensile properties are lower than those obtained with nitrogen atmospheres. The presence of flammable hydrogen requires special handling [18].

1.4.3. Liquid-Phase Sintering

Liquid-Phase Sintering (LPS) is the most used type of sintering. It consists in forming a liquid-phase that enhances material transport and produces great densification at low temperatures. The liquid-phase can be permanent during the high-temperature part of the sintering cycle. It can also be activated by another element, with lower melting point that the major constituent. This is known as activated liquid-phase sintering. In supersolidus LPS, a prealloyed powder is heated to temperatures higher than the solidus to form the liquid phase. A final variant is transient liquid-phase sintering, where the liquid is dissolved into the solid or forms a new phase.

For liquid-phase sintering to be effective, the liquid needs to wet the solid to provide a bonding force between the particles. Solid solubility in the liquid allows reprecipitation, which leads to a more efficient packing of the grains and high densities. It is not desired that the liquid have low solubility in the solid to avoid swelling. Exception of this are in systems that use transient liquid phase, such as Cu-Sn or Cu-Zn.

During LPS, before any liquid is form, there is initially a solid-state sintering which also contributes to densification. Once there is liquid phase present, the capillary forces pulls the liquid into pores and particle necks. This is called rearrangement. A secondary rearrangement occurs when the liquid disintegrates clusters of particles. Depending on a number of characteristics, the dimensional behavior can be either swelling or shrinkage.

The densification is further increased by solution-reprecipitation. Atoms present at convex surfaces in contact with the liquid have greater solubility than those at concave surfaces. Thus, they dissolve and are transported through the liquid and precipitate near concave surfaces. This whole process changes the shape of the grains in a way they can pack better and produce densification. During this stage, there is less dimensional change than during rearrangement. It is the most significant densification mechanism when only small amounts of liquid phase are found.

During the final stage sintering, there is a slow densification of the structure, as well as microstructural coarsening, which can degrade mechanical properties. Trapped gasses can enlarge pores and restrict densification. It can be avoided in vacuum atmospheres.

LPS is usually done with small fractions of liquid phase. High liquid content enhances densification but produce distortion and poor dimensional stability [19].

1.5. Corrosion

The most common type of corrosion is caused by electrochemical reactions between a metal and an aqueous phase. Part of the metal is oxidized and changes to a nonmetallic state. The reactions occur in the surface of the metal, called electrode. It can be uniformly or focus in certain features of the surface of the metal. The liquid conducting the ions is called electrolyte.

Corrosion occurs due to converting the metal into a lower-energy form. It can be known by thermodynamics if a metal is stable. However, it does not inform about the rate of corrosion nor can predict whether corrosion will occur.

The reaction for the formation of aluminium from its ion, Al^{3+}, has a standard potential of -1.66 volts vs. SHE, meaning that thermodynamically aluminium is one of the more reactive metals. However, aluminium forms spontaneously a thin oxide film that protects the metal, thus giving aluminium one an excellent corrosion resistance. Pourbaix diagram for aluminium (see Figure 1.9) shows in what environmental conditions the metal is protected by the oxide layer.

Alloyants have different effects on the oxide film. For example, magnesium forms mixed oxides that enhance the protective properties of the layer. On the other hand, copper weaken the layer, thus the alloys from the 2000 series have lower corrosion resistance [20, 21].

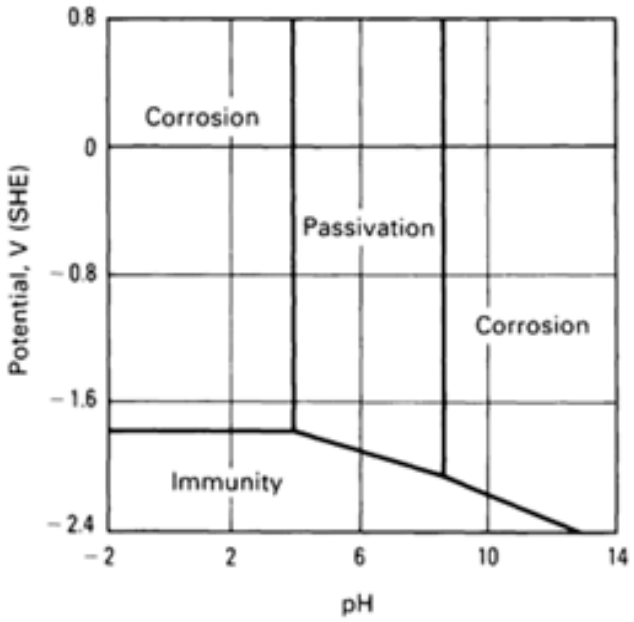

Figure 1.9: Pourbaix diagram for aluminium at 25 ºC [22].

Corrosion control is a high priority concern in the aircraft industry, due to the potential impact on human safety and on expensive aircraft. Materials are required to sustain high levels of payload, thus being chosen more for their mechanical properties than their corrosion resistance. By flying throughout the world, aircraft are exposed to the most severe corrosive environments on earth [23].

Corrosion in aircrafts can appear as local pitting, surface roughening, intergranular and transgranular cracking or degradative transformation of materials (see Figure 1.10). Corrosion problems are related to its interaction with fatigue, wear, erosion and stress, resulting in premature fracture.

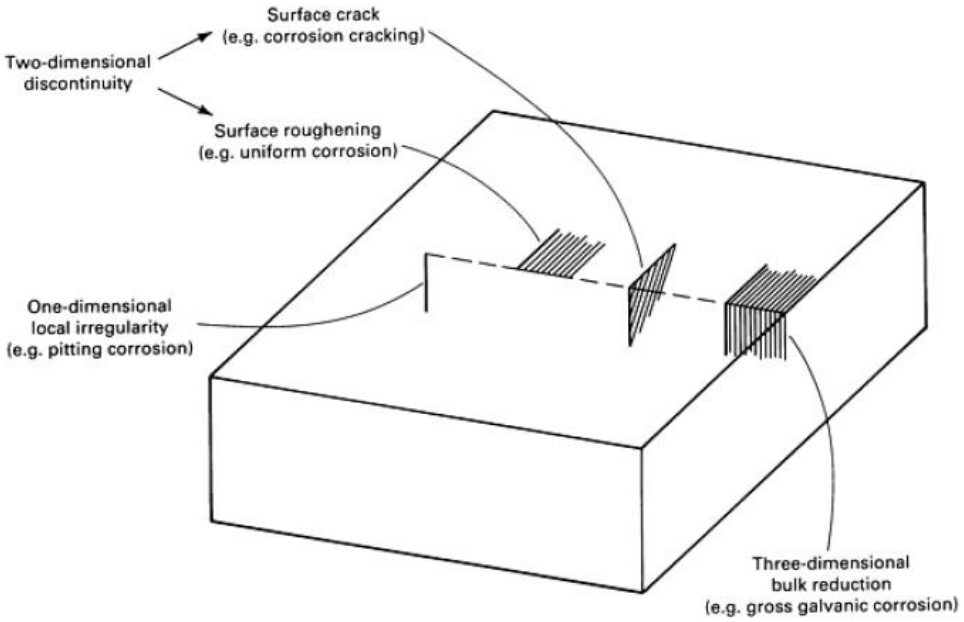

Figure 1.10: Physical effects of corrosion on metallic aircraft materials [23].

1.5.1. Pitting corrosion

Pitting corrosion is an extremely localized corrosive attack. While aluminium's passive film provides the metal with an excellent corrosion resistance, it is susceptible to localized breakdowns. As a result, an electrolytic cell is formed, with the anodic area being a small area of active metal and the cathode a much larger area of passive metal. The small anode is rapidly corroded, forming a pit that penetrates the metal.

Pitting corrosion of aluminium occurs in the presence of chloride ions. At weak points of the film, microcracks of few nanometers wide are formed. Most of them stop growing and repassivate, but a small fraction of them propagate. In those, at the bottom of the pit aluminium is oxidized (1.1) and the electrons move through the metal.

$$2\ Al \rightarrow 2\ Al^{3+} + 3e^- \quad (1.1)$$

Outside the cavity, these electrons cause the reduction of water (or formation of hydrogen, in acid solutions):

$$2/3\ O_2 + 3\ H_2O + 6e^- \rightarrow 6\ OH^- \quad (1.2)$$

or

$$6\ H^+ + 6e^- \rightarrow 3\ H_2 \quad (1.3)$$

The overall reaction is the formation of aluminium hydroxide:

$$2\ Al + 3\ H_2O + 3/2\ O_2 \rightarrow 2\ Al(OH)_3 \quad (1.4)$$

The presence of the aluminium ions at the bottom of the pit attracts chloride ions to neutralize the solution and form aluminium chlorides. Hydrogen ions are formed due to hydrolysis (1.5) of the aluminium chlorides, lowering the pH below 3 at the bottom of the pit. The aggressiveness of the resulting environment stimulates further corrosion (see Figure 1.11).

$$Al^{3+} + 3\ H_2O \rightarrow Al(OH)_3 + 3\ H^+ \qquad (1.5)$$

The hydrogen ions forming hydrogen bubbles push the precipitated aluminium hydroxide to the opening of the pit, progressively blocking the entry and slowing or even stopping the corrosion process.

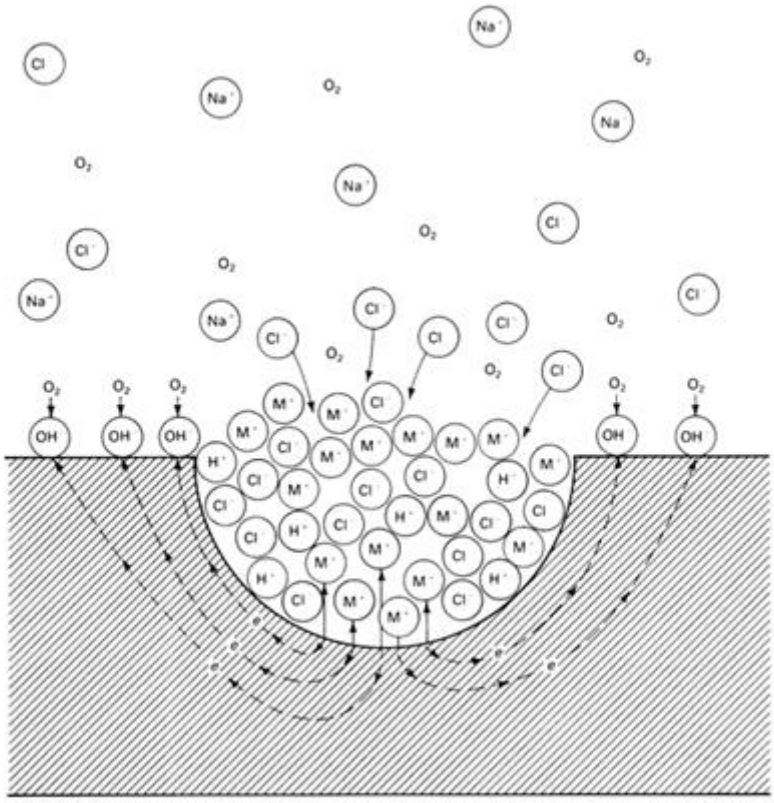

Figure 1.11: Diagram of pitting corrosion in a disolution containing NaCl. The higher concentration of Cl^- and H^+ in the pit stimulates the corrosion process [24].

Pitting corrosion resistance can be measured with immersion tests, which allow direct comparison between alloys and correlate with service experience. Advanced electrochemical techniques can also be used to test pitting corrosion [22, 24, 25].

The presence of cathodic intermetallics, such as Al_2Cu, weaken the passive film and are sites for pit nucleation. Intermetallic particles are generally considered to be the initiation sites of localized corrosion due to creating flaws in the oxide surrounding these particles, as well as having different potential compared to the matrix. They produce a galvanic cell with the aluminium matrix and oxygen can reduce in them. The particles can dissolve, which can result in metallic elements, such as Cu, that are even more cathodic than the intermetallics [26-28].

1.5.2. Electrochemical Impedance Spectroscopy (EIS)

Electrochemistry is the part of the chemistry that deals with the relationship between electricity and chemical reactions that produce or consume electric energy.

Eletrochemical techniques are the most used to determine materials resistance to corrosion, due to being fast and simple. They are based on analyzing the response of an electrochemical system to a known perturbation of voltage or current. One the different electrochemical techniques, Electrochemical impedance spectroscopy, has experience an incredible development in the last years and is now a powerful tool for studies of degradation of organic coatings and metallic corrosion [29].

EIS consists in applying a sinusoidal signal of variable frequency that perturbs the system, obtaining another sinusoidal signal as response. For example, we could apply a potential signal:

$$E = E_0\, sen\, (\omega t) \tag{1.6}$$

By varying the frequency, ω, from zero to infinity we can obtain the response of the system as a current signal, i. In a linear system and in permanent regime conditions, the response to a sinusoidal excitation signal is another sinusoidal signal, with the same frequency but a difference of amplitude and phase:

$$i = i_0\, sen\, (\omega t + \phi) \tag{1.7}$$

with E_0 and i_0 being the maximum amplitude of the input and output signals, respectively, and ϕ the difference of phase between them. For the system to remain lineal and to not provoke any irreversible modifications due to measuring, the maximum amplitude of the input signal tends to be quite low, of magnitudes close to 10 mV.

The relationship between the potential applied and the output current is known as the system impedance. Its argument is the difference in phase ϕ and its modulus is the quotient between the amplitudes of the potential input signal and the output current signal:

$$|Z| = E_0/i_0 \tag{1.8}$$

Impedances can be represented in complex notation, which allows the representation of the impedance vector in the complex plane, also known as Argand diagram (Figure 1.12).

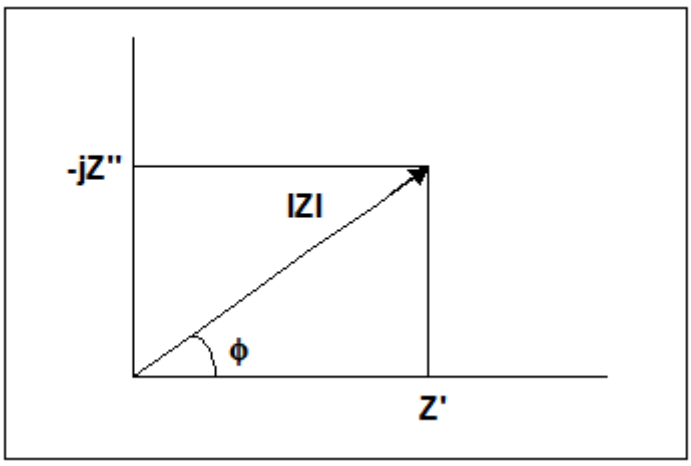

Figure 1.12: Representation of the impedance vector in an Argand Diagram [29].

The impedance is a function of the frequency, with both Z' and Z'' acquiring new values depending on the frequency of the signal. To represent the different values of Z from frequencies zero to infinity, a diagram of Nyquist is traced (Figure 1.13).

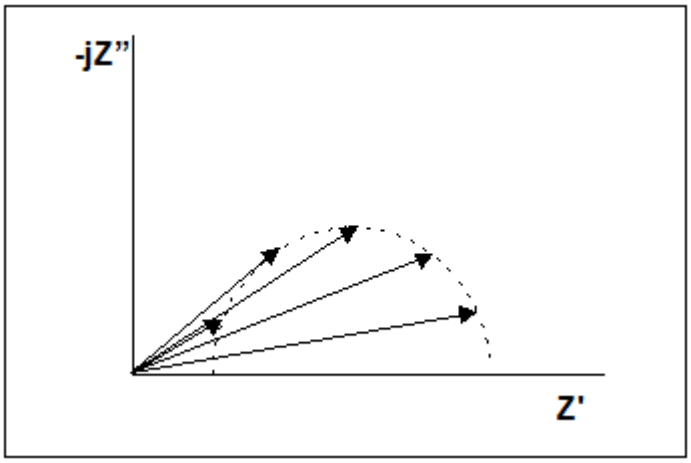

Figure 1.13: Nyquist diagram of the impedances [29].

To analyze the variation of the impedance of an electrochemical cell with the frequency, a equivalent circuit can be used. It is composed of electric elements that behave as the electrode studied. Thus, a simple electrochemical system can be represented by a resistance in parallel with a capacitor (simulating the interface electrode/electrolyte), with both being in series with another resistance, as can be seen in Figure 1.14. This circuit is known as equivalent circuit of Randles and it correlates quite well with most electrochemical systems.

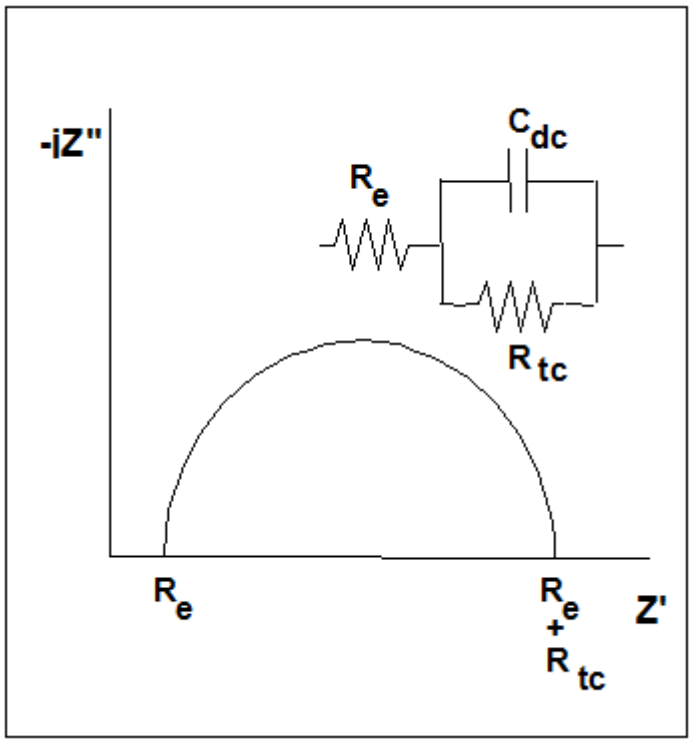

Figure 1.14: Simplified equivalent circuit of Randles and its frequency response represented as a Nyquist diagram [29].

R_e represents the ohmic resistance between the working electrode and the reference electrode, including the electrolyte and surface layers resistance. C_{dc} is the capacity of the double electrochemical layer formed in the interphase electrode/electrolyte, and, lastly, R_{tc} represents the charge transference ion/electron used to determine the speed of the electrochemical reaction when the system is controlled by activation.

The Nyquist diagram can be used to determine the different elements of the circuit. R_e is the value in the real axis at high frequencies, R_{tc} is the diameter of the semicircumference, and C_{dc} can be obtained using the following equation:

$$C_{dc} = -\frac{1}{\omega_{max} R_{tc}} \tag{1.9}$$

with ω_{max} being the maximum frequency applied.

At low frequencies, the diffusion impedance enters into effect as a consequence of the concentration variations produced by the actions of the alternate field and the transport of mass in the interphase and its surroundings. To take it into account, an additional impedance, Z_w, known as Warburg impedance, is added in series with R_{tc} and parallel with C_{dc}. Its value depends on the frequency and comes from the following equation:

$$Z_w = \frac{\sigma w}{\omega^{\frac{1}{2}}}(1 - j) \tag{1.10}$$

with σw being the Warburg diffusion coefficient, that depends on the concentration of the oxides and reduced species of the system, the chemical diffusion coefficients, temperature and the number of electrons involved in the process.

The resulting equivalent circuit and its frequency response are represented in Figure 1.15.

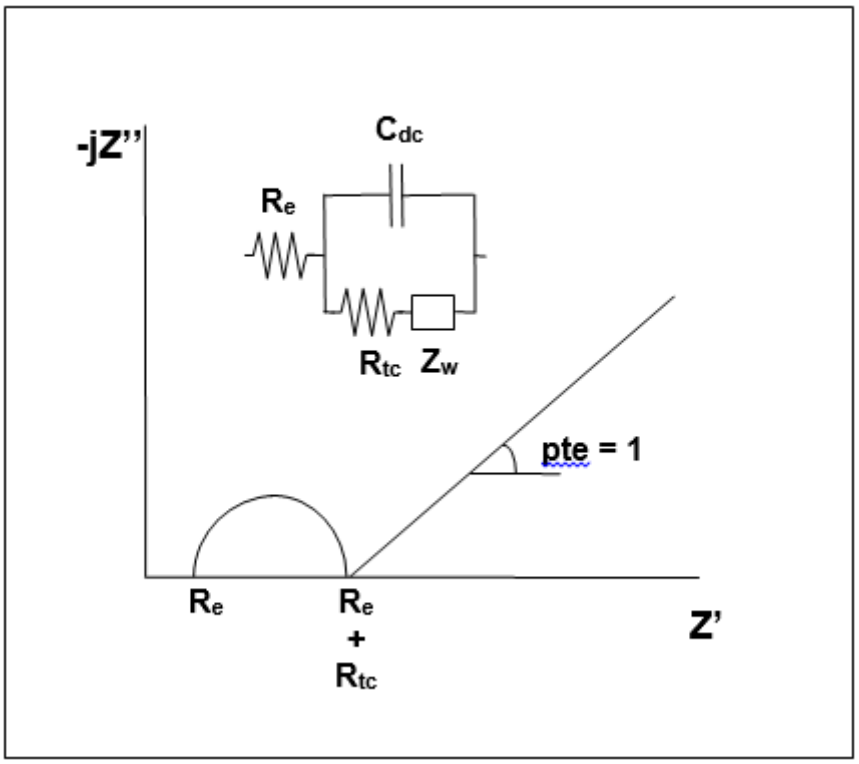

Figure 1.15: Equivalent circuit with the Warburg diffusion impedance [29].

CHAPTER 2: MATERIALS AND EXPERIMENTAL

In this project, a characterization and optimization of a P/M manufactured AA2014 alloy has been carried out (see Figure 2.1). It includes the following tasks:

- Characterization of prealloyed AA2014 powder, through the usage of SEM, XRD and laser diffraction.
- Mixing of the powder with lubricant and uniaxial die compaction at three different pressures.
- Characterization of the green compacts, measuring density and bending strength.
- Sinterization and heat treatment
- Characterization of the finished samples, including physical and mechanical properties such as density or hardness, microstructure and corrosion resistance.

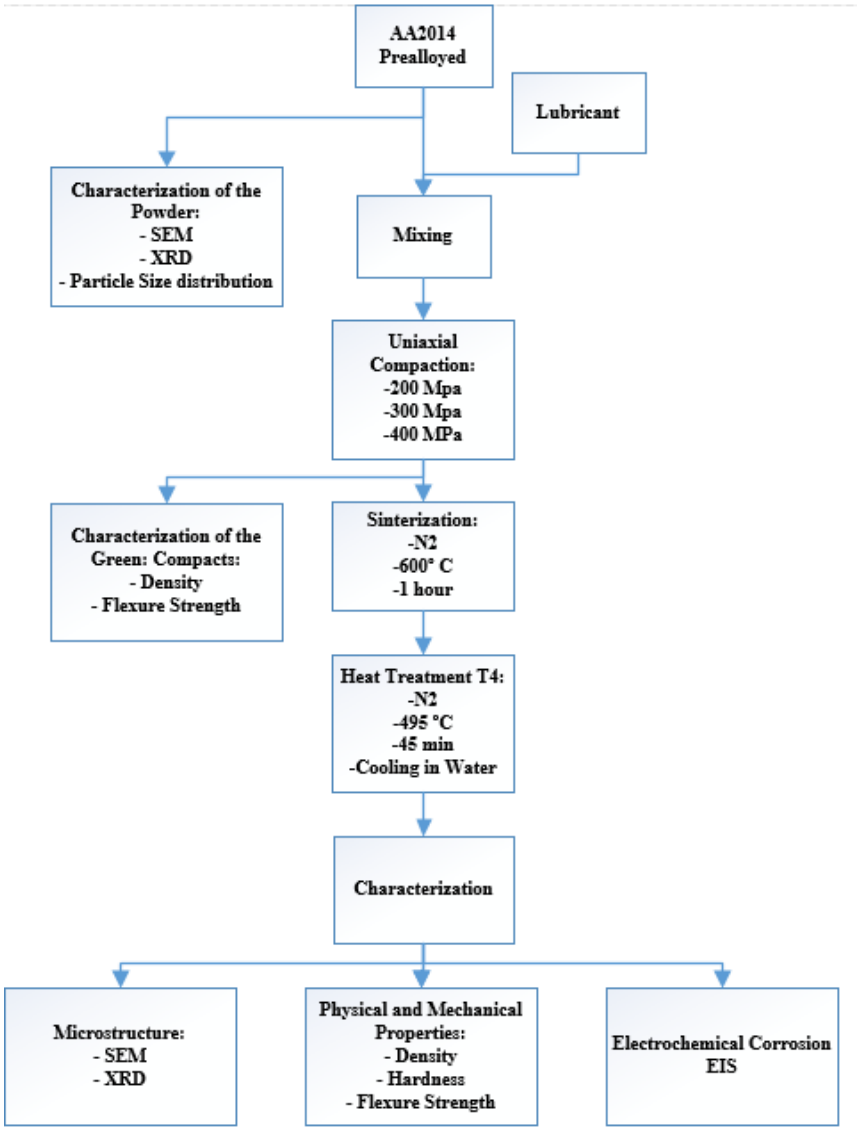

Figure 2.1: Experimental procedures.

2.1. Powder characterization

The starting material is prealloyed AA2014 powders provided by The Aluminium Powder Co. LTD. The expected composition is as shown in Table 2.1.

Table 2.1: AA2014 Composition.

Element	Weight percentage
Si	0.50-1.2
Fe	0.7
Cu	3.9-5.0
Mn	0.40-1.2
Mg	0.20-0.8
Cr	0.10
Zn	0.25
Ti	0.15
Al	Remaining

To characterize the powders, studies of their particle size distribution, shape and chemical composition have been carried out.

2.1.1. Particle size distribution

Particle size distribution were determined by laser diffraction using the equipment Malvern Mastersizer 2000/2000E. A sample of the powder is dispersed in an aqueous form, water for this case, and agitated at 2000 rpm. The particles are pumped in front of a laser beam. Measuring the diffraction of the laser beam, particle size distribution can be measured.

Laser diffraction (or light-scattering) is a fast, easy to use and reproducible way of measuring particle size. It can also measure in a high range of sizes, from 0.01 μm to mm.

The results are a histogram of every size and the cumulative plot.

2.1.2. Shape

A Scanning Electron Microscope (SEM) has been used to observe the shape of the powders. The machine utilized is a Philips XL-30, with a Tungsten filament equipped with an analyzer EDAX DX-4 for energy-dispersive X-ray spectroscopy (EDX). The voltage used was 15-20 kV for the capture of backscattered electron images.

The sample was powder packed in conductive resin to carry out the experiment.

2.1.3. Chemical composition

The chemical composition of the powders was studied using X-rays crystallography. An x-ray beam impacts our sample and diffracted into specific directions. The intensity of the diffracted

beam is measured. It depends on the angle of impact between the beam and the sample, and on the molecular structure of the crystals of the sample. Comparing the intensity peaks with a database, it is possible to know what compounds are present in the sample.

The equipment utilized was an X-Pert Philips diffractometer. The experiment was carried out at 40 kV and a current of 40 mA. The intensity was measured at angles ranging from 10º to 90º, making measures each 0.02º. The database utilized to identify the intensity peaks was the one available in the Departamento de Ciencia e Ingeniería de Materiales e Ingeniería Química de la Universidad Carlos III de Madrid.

2.2. Uniaxial die compaction

The powder is mixed first with Acrawax in a 1.5% in weight. The lubricant was necessary to prevent the samples from delaminate during compaction. A turbula WAB type T2F NR 030133 was used, with 230 V of voltage, a frequency of 50 Hz and a power of 0.18 kW.

The compaction was performed in a Microtest ECH/1500/H model hydraulic press of 1500 kN capacity. Three different compaction pressures chosen: 200 MPa, 300 MPa and 400 MPa [30, 31].

2.3. Green compact characterization

Green compacts were tested in two different things: density and bending strength.

2.3.1. Green density

The technique used to measure density is based on the Archimedes' principle, according to the norm ISO 2738 [32]. The samples are weighted, then sealed with a resin and weighted again. The experiment is carried out by immersing the sealed sample in water and weighting it. Since it is sealed, the water cannot fill the open pores. Equation 2.1 is then used to obtain the density.

$$\rho = \frac{Mass\ without\ resin(g)}{\left(\frac{Mass\ with\ resin(g) - Mass\ immersed(g)}{Water\ density\ (\frac{g}{cm^3})}\right) - \left(\frac{Mass\ with\ resin(g) - Mass\ without\ resin\ (g)}{Water\ density\ (\frac{g}{cm^3})}\right)} [\frac{g}{cm^3}] \quad (2.1)$$

The sealant resin has a density of 1.200 g/cm3 and the water, at 20 ºC, a density of 0.997 g/cm3.

Relative density can be calculated with:

$$\rho_r = \frac{\rho}{\rho_{theorical}} \cdot 100[\%] \quad (2.2)$$

The theoretical density of AA2014 is 2.80 g/cm^3 at 20 ºC [8].

Finally, with this experiment we can also calculate residual porosity:

$$P_T = 100 - \frac{\rho}{\rho_{theorical}} \cdot 100[\%] \quad (2.3)$$

2.3.2. Bending strength

Bending strength of the green compacts was measured using a three-point flexure test according to the ISO 3325:2002 norm [33]. The measure was realized in a MicroTest machine that shows the maximum force the compact sustained before breaking. With that value and the sample dimensions, as well as the distance between points, we can calculate the flexural strength of the matrix with the following formula:

$$\sigma = \frac{3 \cdot F(N) \cdot L(mm)}{2 \cdot t^2\ (mm^2) \cdot w\ (mm)} [\frac{N}{mm^2}] \quad (2.4)$$

with F being the maximum force, L the distance between supports, and t and w the sample thickness and width, respectively.

2.4. Sintering and heat treating

The sintering cycle and heat treatment were chosen based on previous studies [34-37] and supported by two different experiments: an analysis of the phase diagram of the alloy and a thermogravimetric analysis of the powder.

The phase diagram shown in Figure 2.2 was obtained using the software Thermo-calc available at Universidad Carlos III de Madrid. Thermo-calc is able to represent phase diagrams of complex alloys. The diagram was represented as a function Cu, with 0.8 Si, 0.8 Mn and 0.5 Mg, in weight percentage. In addition, Thermo-calc can also represent a diagram (Figure 2.3) with the solid and liquid proportions of an alloy (Cu content taken as 4.4 wt %) during a heating or cooling process.

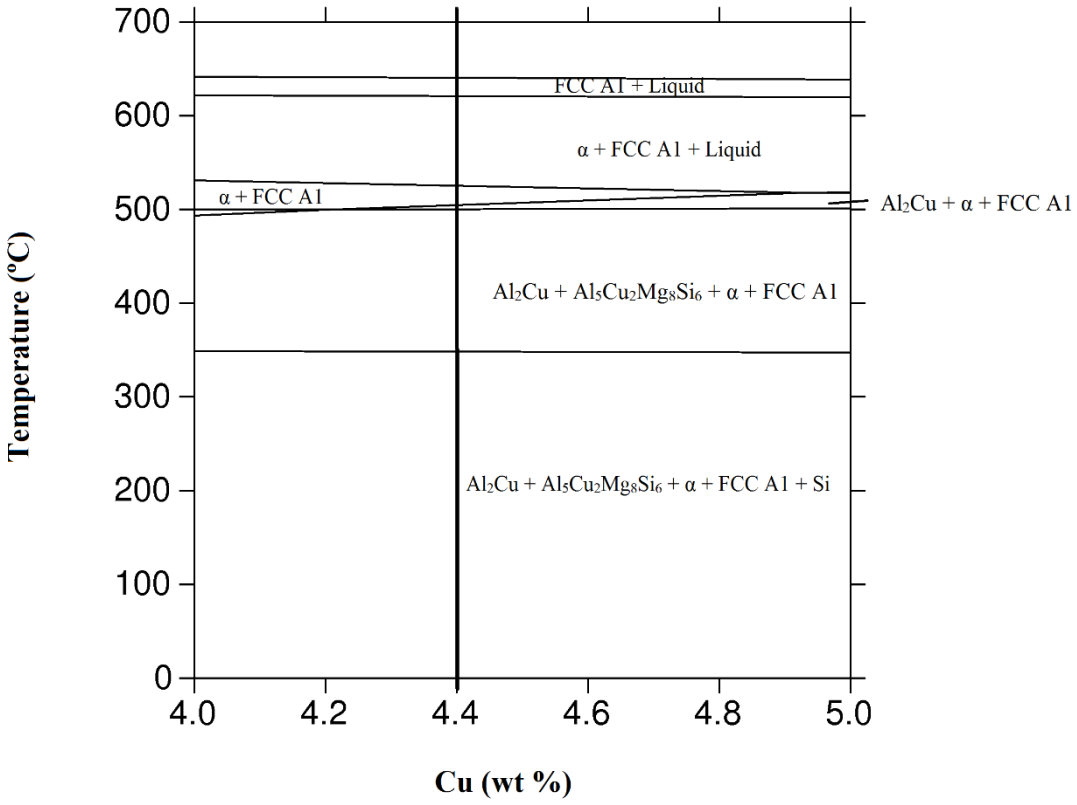

Figure 2.2: Phase Diagram of Al-Cu alloy, with fixed contents of Si (0.8), Mn (0.8) and Mg (0.5).

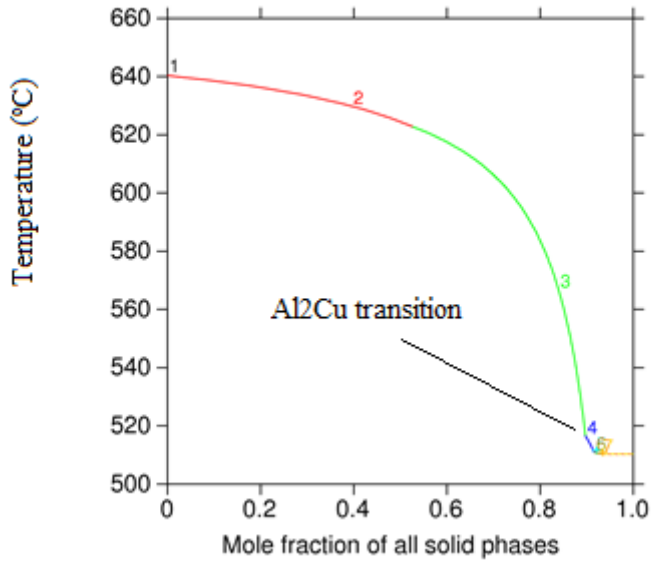

Figure 2.3: Fraction of solid phase during a cooling process.

Liquid phase appears at temperatures above 500 ºC, with Al2Cu turning into liquid at temperatures of 510 ºC. Thus, in order to have liquid phase aiding the sintering process, we will require temperatures higher than 510 ºC.

The thermogravimetric analysis (TGA) shows us two things:

- The burn off of the lubricant, occurs in the range of temperatures of 200 to 400 ºC. The mass loss correlates with the quantity of lubricant added, i.e. 1.5 in weight percentage. (Figure 2.4)

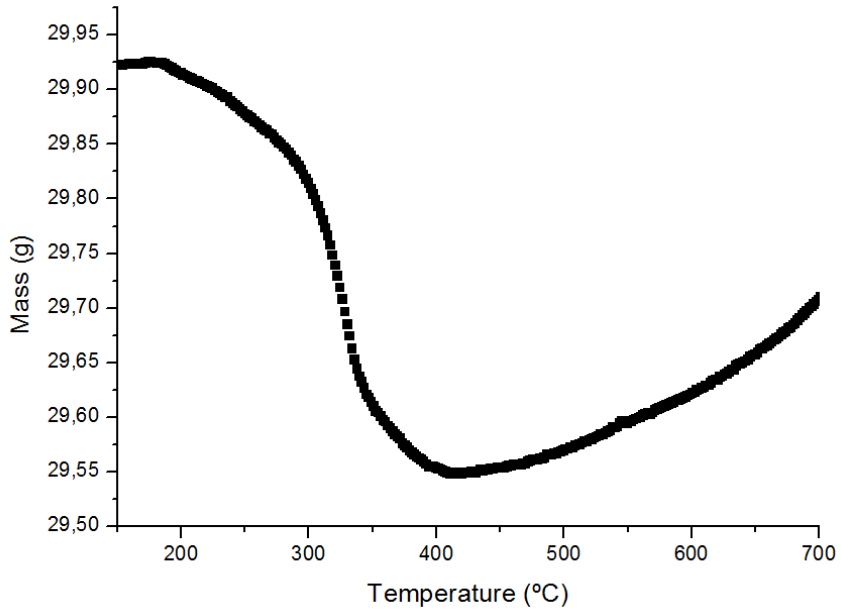

Figure 2.4: Thermogravimetric analysis showing the variation of mass with temperature.

- An endothermic peak at around 640 ºC, corresponding to the fusion, which confirms what we saw using Thermo-Calc. (Figure 2.5)

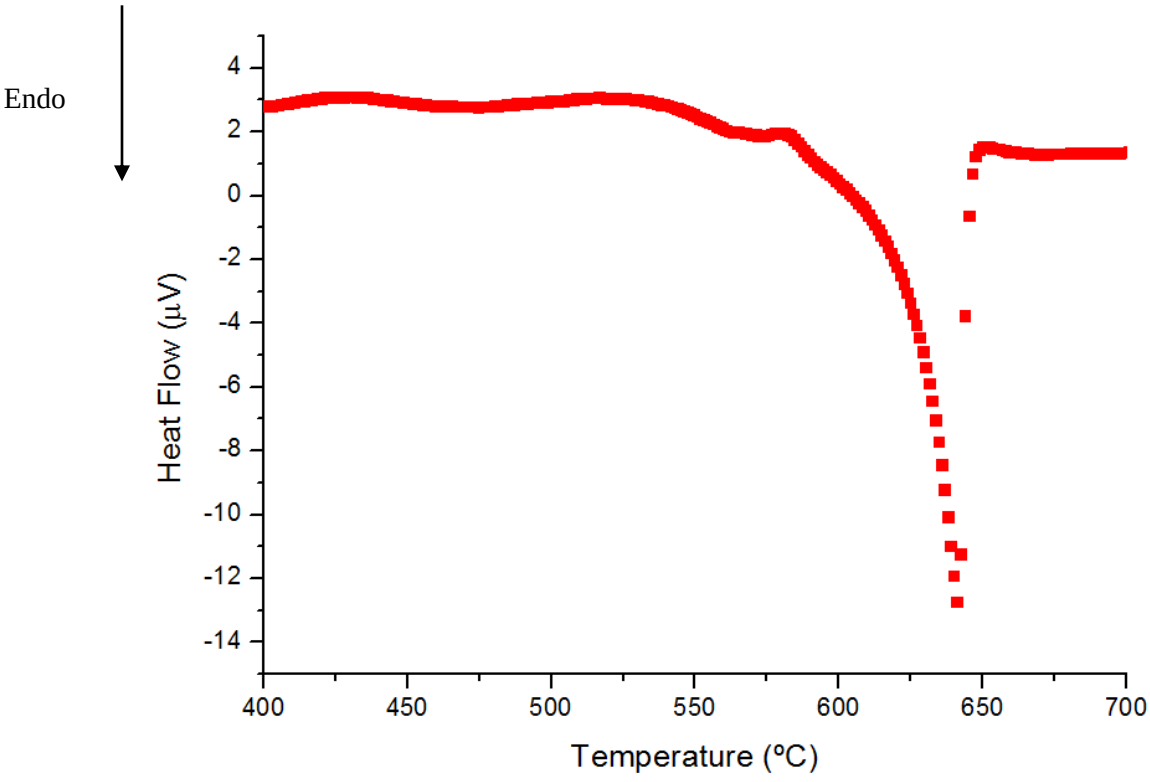

Figure 2.5: Thermogravimetric analysis showing heat flow variations with temperature.

With the information available, a plateau at 600 ºC for 1 hour was chosen for the sintering cycle. At that temperature, the liquid fraction is expected to be around 25% in moles, enough to achieve a good densification. A heating rate of 5 ºC/min allows the correct burn off of the lubricant. See Figure 2.6.

The heat treatment, T4, starts with a solution heat treating at 495 ºC for 1 hour with a water quenching for cooling. The aging occurs naturally during the following 7 days. See Figure 2.7. This heat treatment was chosen based on previous studies [34-37] and it is commonly used for precipitation strengthened alloys.

The atmosphere during both the sintering and the heat treatment was Nitrogen. As explained in the introduction, nitrogen is an inexpensive inert gas that protects aluminium from oxidation and helps breaking the oxide layer to allow sintering [34-37].

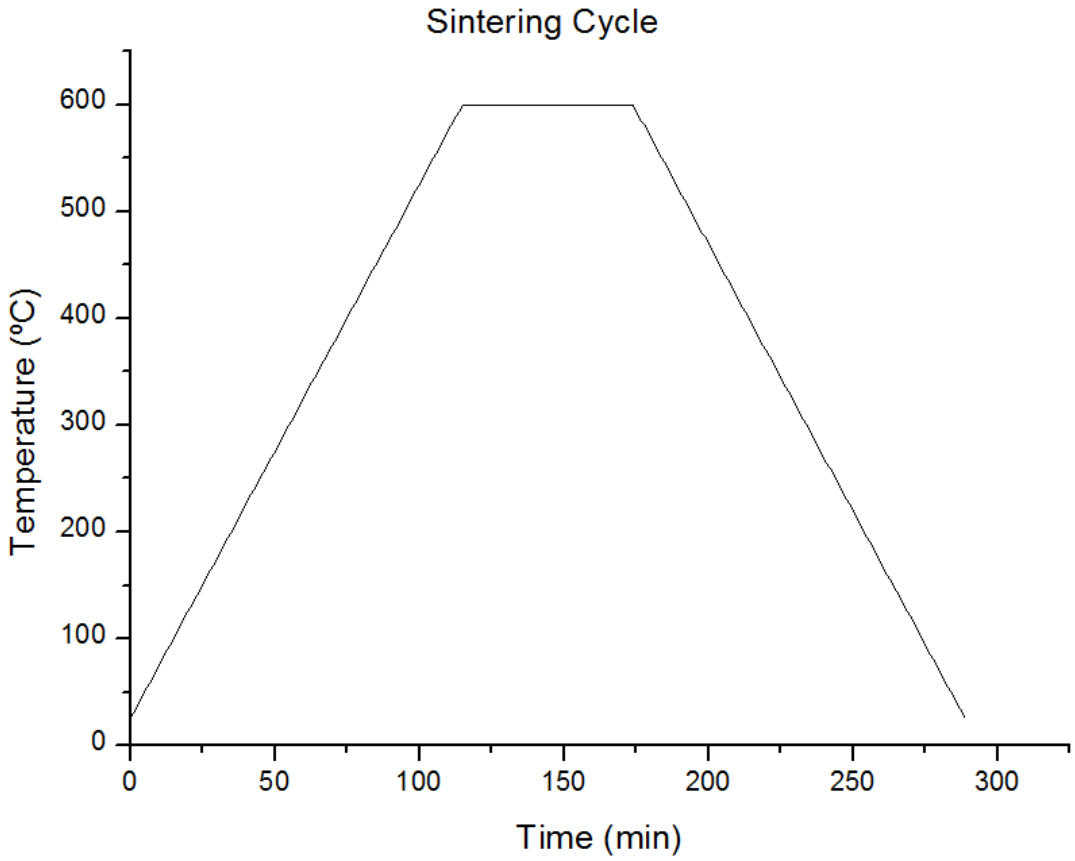

Figure 2.6: Sintering Cycle.

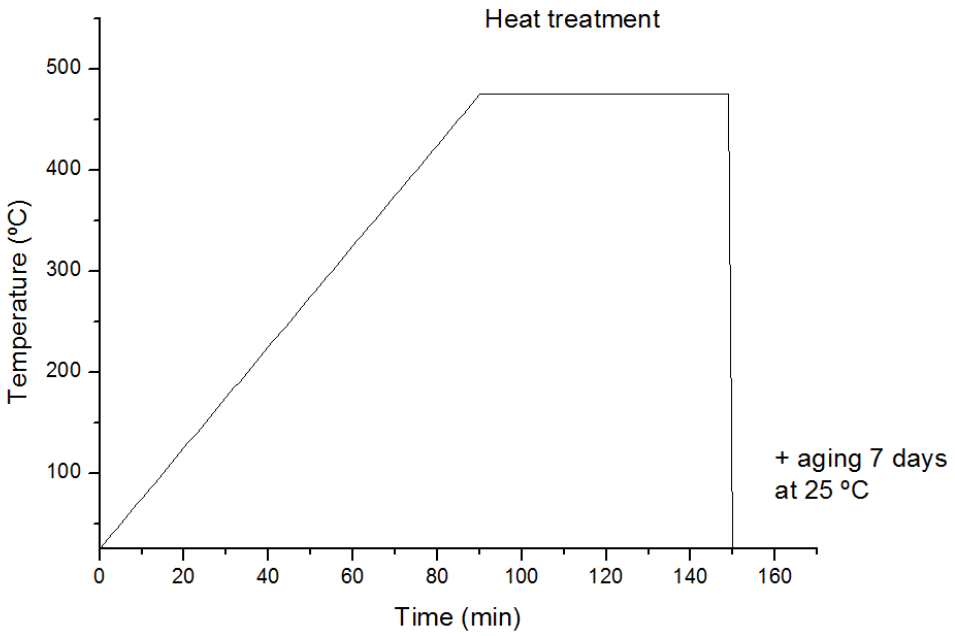

Figure 2.7: Heat treatment.

2.5. Characterization of heat treated samples

As with the green samples, properties of the sintered and heat treated samples were measured. Additionally, the microstructure of the samples was analyzed.

2.5.1. Physical properties

Similar to the green samples, density and flexure strength were measured, following the same procedures than in the previous case.

In addition, hardness was also measured using a Wilson Wolpert Universal Hardness DIGI-TESTOR 930. The hardness determined was the HV10 by applying 10 kg. The procedures were carried out according to the norm ISO 6507/1 [38].

2.5.2. Microstructural properties

Three different techniques were used to determine the microstructure of the samples:

- X-rays diffraction crystallography:

  As with the powders, X-rays crystallography provides information about the different crystalline phases present in the sample by showing intensity peaks at different angles. The angles can later be compared to a database, thus identifying what phases are present.

  The samples were cut transversally using a Minitom equipment and a diamond blade spinning at 300 rpm, with water as coolant.

- Scanning Electron Microscopy:

  SEM provides additional information about the phases present. The sintered and heat treated in the sample were cut and packed in a conductive resin and refined using sandpaper of SiC of different sizes (600 and 1000) and polished with alumina suspensions of sizes 9, 1 and 0.3 μm.

2.6. Electrochemical corrosion: Electrochemical Impedance Spectroscopy (EIS)

The sinterized and heat treated samples were immersed in a diluted Harrison solution of 0.05% weight NaCl and 0.35% wt $(NH_4)_2\ SO_4$. A conventional three-electrode configuration was used: a reference electrode made of Ag/AgCl, a platinum wire as counter electrode and, as working electrode, the aluminium samples. Measures were taken at ambient temperature and at different times, ranging from 1 to 24 hours. For that purpose, a Faraday cage was used, with a PGSTAT302N potentiostat and a FRA32M module, both from Metrohm Autolab (EcoChemie).

The sample area exposed was 0.63 cm^2 and the range of the frequency applied between 10^5 and 10^{-2} Hz. The impedance spectrums were registered at open circuit voltage, applying logarithmic sweeps of 5 points per decade and a sinusoidal perturbation of ±10 mV of voltage.

The impedance spectrums can be used to know the physicochemical processes that are occurring in the immersed sample, through the use of adequate equivalent circuits. The results obtained from EIS has been adjusted using the program Zview®.

CHAPTER 3: RESULTS AND DISCUSSIONS

3.1. Powder characterization

3.1.1. Particle size distribution

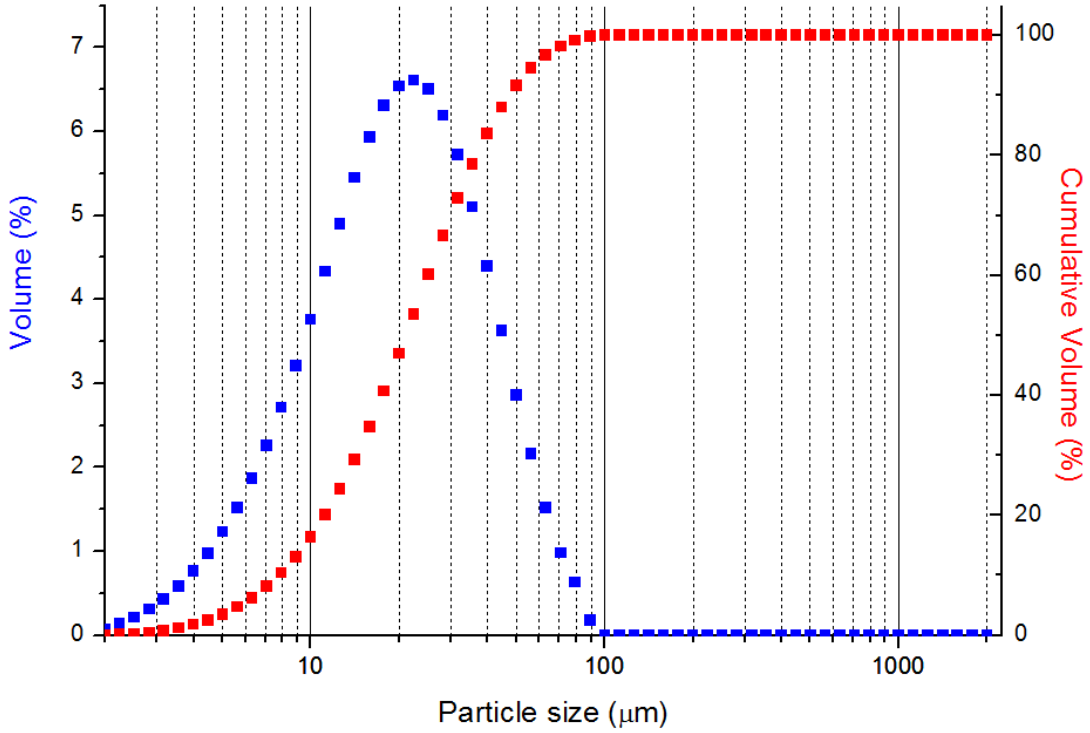

Figure 3.1: Particle size distribution of prealloyed powder .

The prealloyed powders show a mean particle size of 21.1 µm. However, the distribution of size of the powder ranges from less than 10 µm to almost more than 50 µm. Table 3.1 shows the D10, D50 and D90 indexes, which represent the size at which the cumulative volume reaches 10%, 50% and 90%, respectively. This size of powders can be obtained through gas atomization [39].

Table 3.1: D10, D50 and D90 Indexes for particle size distribution of the powders.

	D10 (µm)	D50 (µm)	D90 (µm)
AA2014	7.823	21.100	47.524

3.1.2. Particle Shape

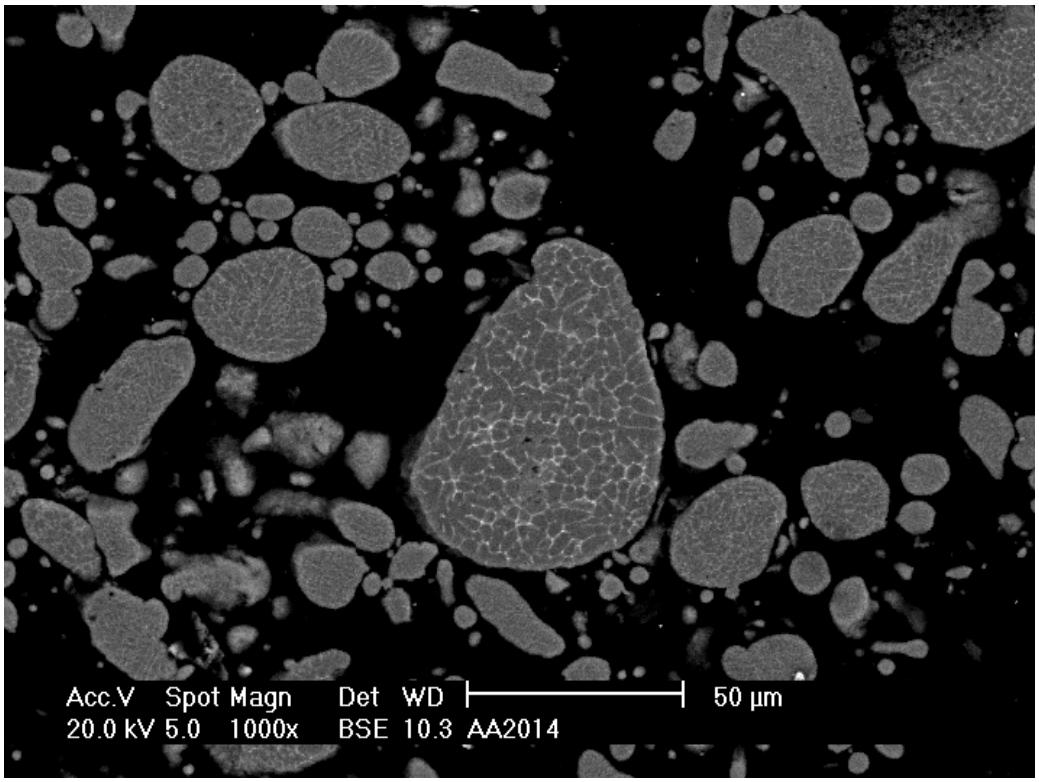

a

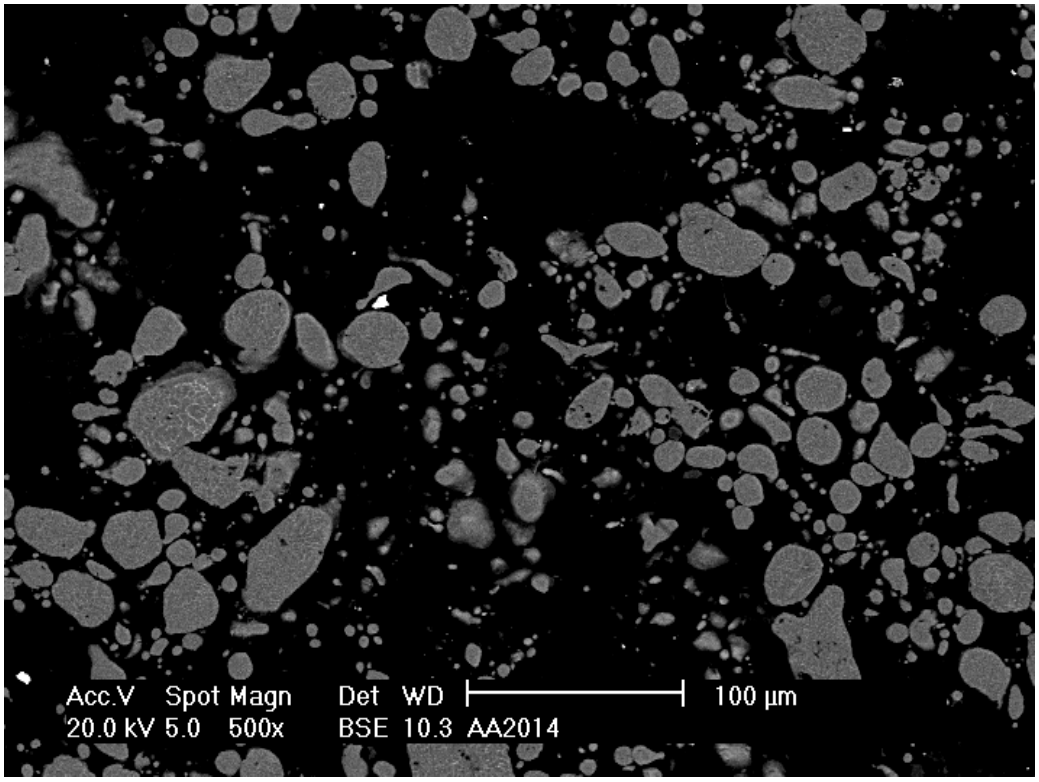

b

Figure 3.2: SEM images of the Powder at 1000x (a) and 500x (b) magnifications.

The powder particles observed in Figure 3.2 present a rounded/spherical shape, with satellites present in some cases [40]. The figure shows the cross section of the powder, allowing the Copper to be seen inside the particles in a white color.

3.1.3. Powder composition

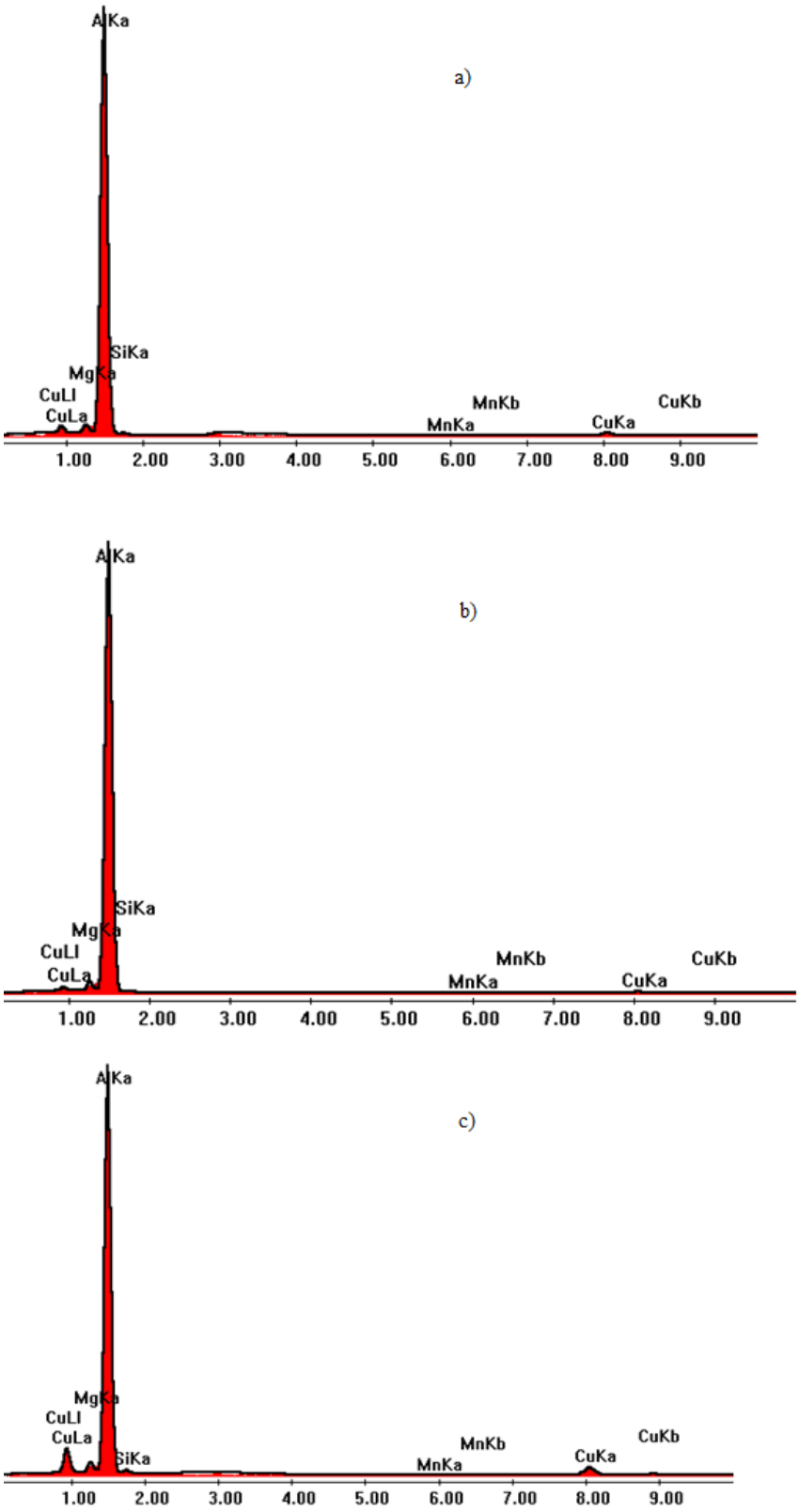

Figure 3.3: EDX analysis of the powder composition at the matrix (a, b) and at the white precipitates (c).

Figure 3.3 shows the composition of the powder in its different zones. Obtained through EDX analysis while observing the samples through SEM. The results are a high Al content, as expected, with image c), taken in one of the white precipitates showing a higher Cu content that indicates the presence of a Al-Cu intermetallic.

X-Rays Diffraction (XRD)

The XRD analysis results can be seen in Figure 3.4. The five main planes (Table 3.2) of aluminium alpha phase (REF Code: 00-001-1180) can be seen clearly. Another phase that can be identified is the intermetallic Al_2Cu (REF Code: 00-002-1309) (Table 3.3). The size of their peaks compared to those from the alpha phase of aluminium indicate that the precipitate is only present in a small proportion.

Table 3.2: Aluminium Alpha phase main peaks.

2θ	38,610	44,833	65,186	78,306	82,352
Relative intensity (%)	100	40	30	30	7
Plane's Miller index	(111)	(200)	(220)	(311)	(222)

Table 3.3: Al_2Cu phase main peaks.

2θ	20,688	29,063	37,934	42,612	47,569
Relative intensity (%)	48	22	46	73	100
Plane's Miller index	(110)	(200)	(211)	(112)	(310)

Both experiments indicate that the Cu content in the alloy should be as expected for an AA2014 alloy according to Table 2.1 and that is forming an Al_2Cu intermetallic.

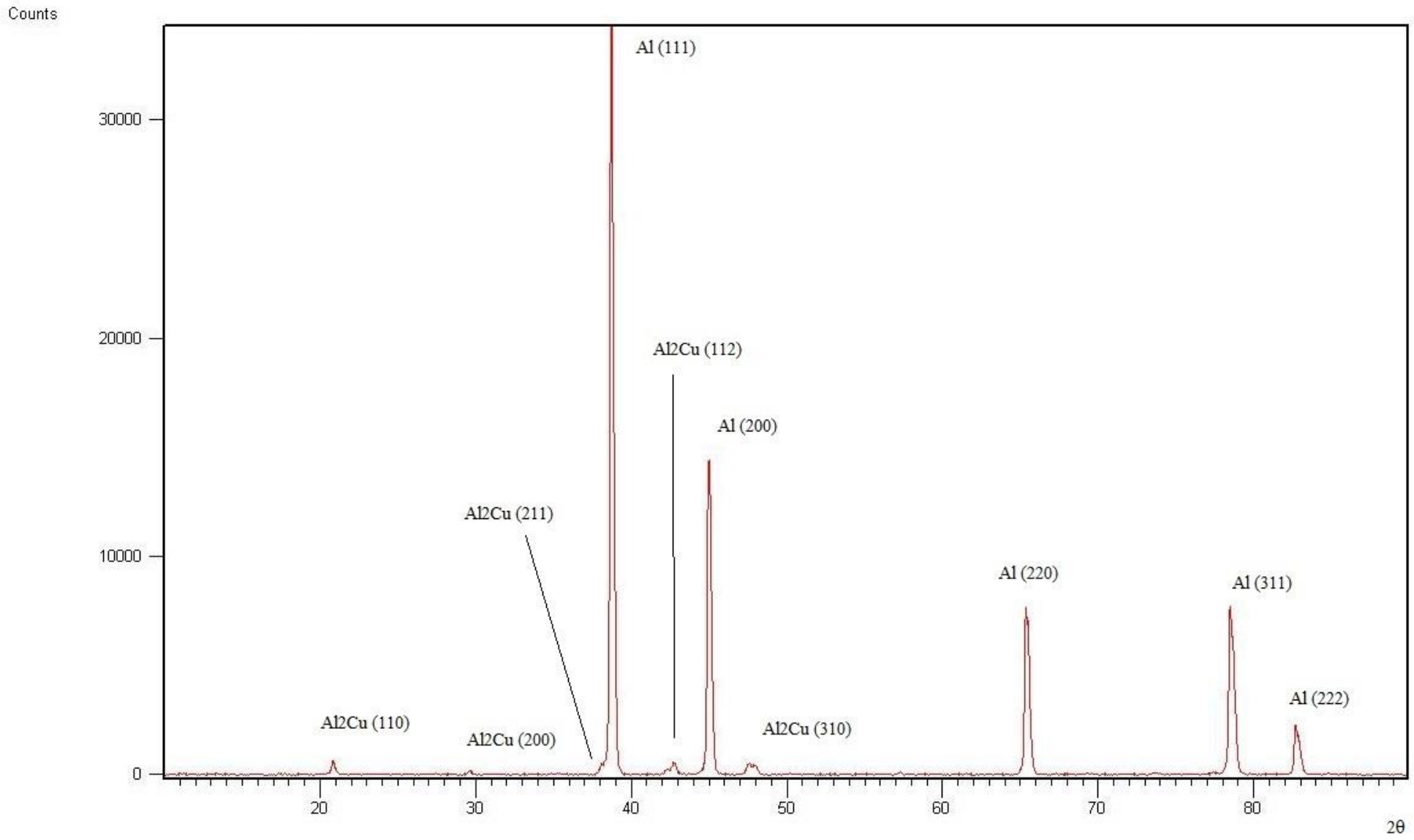

Figure 3.4: XRD analysis of the powder, showing the pressence of the phase Al_2Cu.

3.2. Green characterization

3.2.1. Green density

After the uniaxial die compaction, the average green density (g/cm3) obtained was 2.22, 2.28 and 2.37 for compaction pressures of 200, 300 and 400 MPa, respectively, as can be seen in Figure 3.5 and Table 3.4. Some of the 200 MPa samples failed to compact adequately.

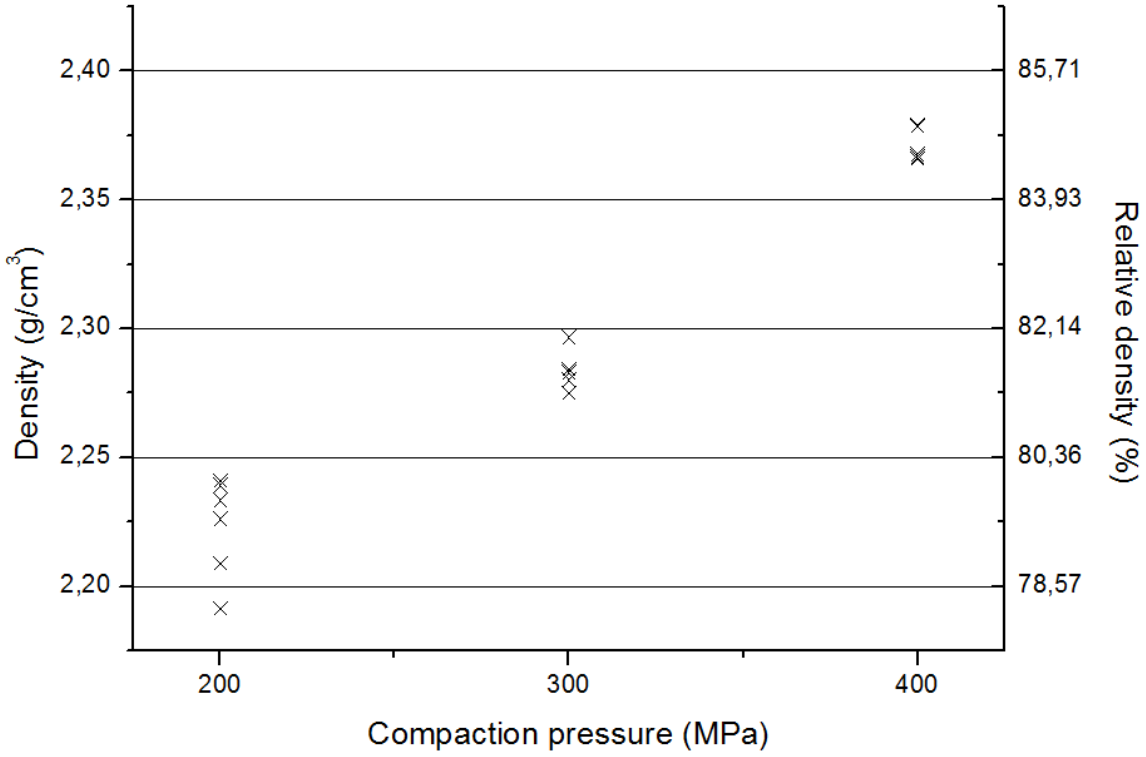

Figure 3.5: Green density.

Table 3.4: Green density.

Compaction Pressure (MPa)	Density (g/cm^3)	Standard Deviation (g/cm^3)	Relative density (%)	Porosity (%)
200	2.22	0.020	79.40	20.60
300	2.28	0.008	81.56	18.44
400	2.37	0.007	84.70	15.30

3.2.2. Bending strength

The same samples whose density was measured were used for the bending strength in three points. The samples dimensions were of the order of 31.7 to 12.7 to 2.8 mm^3. Results can be seen in Figure 3.6 and Table 3.5.

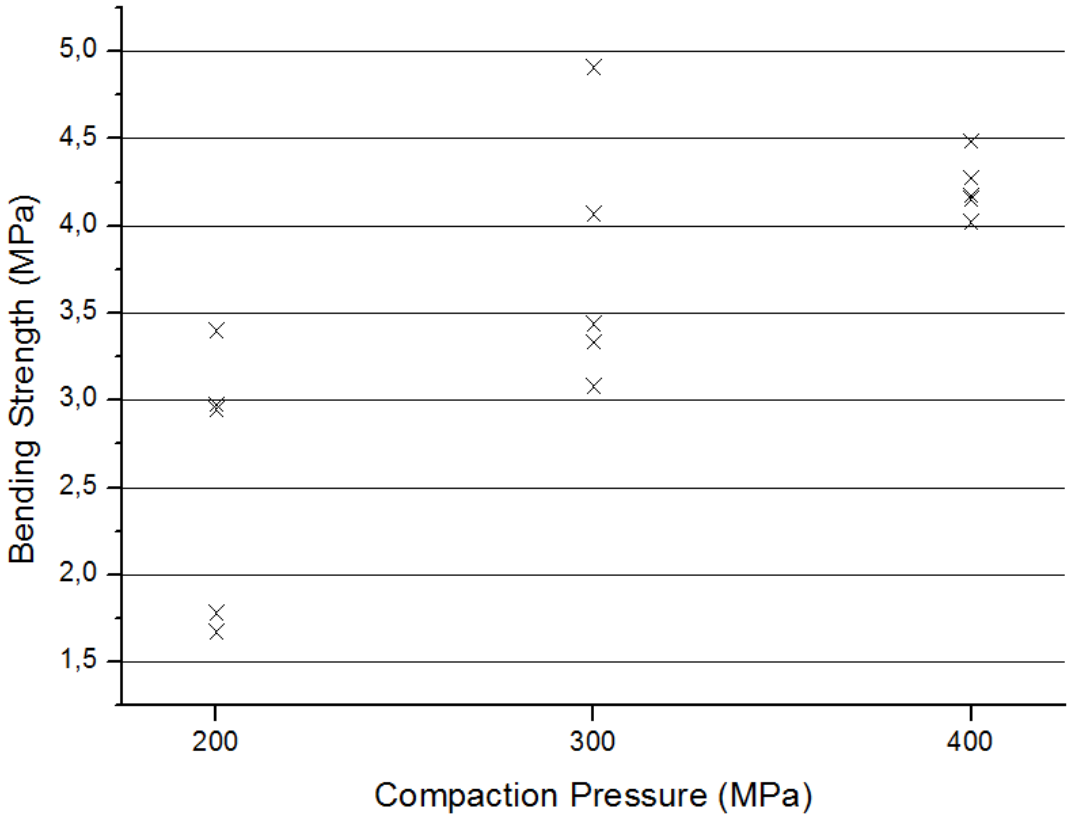

Figure 3.6: Bending strength of Green samples.

Table 3.5: Average Green bending strength .

Compaction Pressure (MPa)	Bending strength (MPa)	Standard Deviation (MPa)
200	2.55	0.78
300	3.76	0.73
400	4.22	0.17

3.3. Sintered and Heat treated characterization

3.3.1. Density

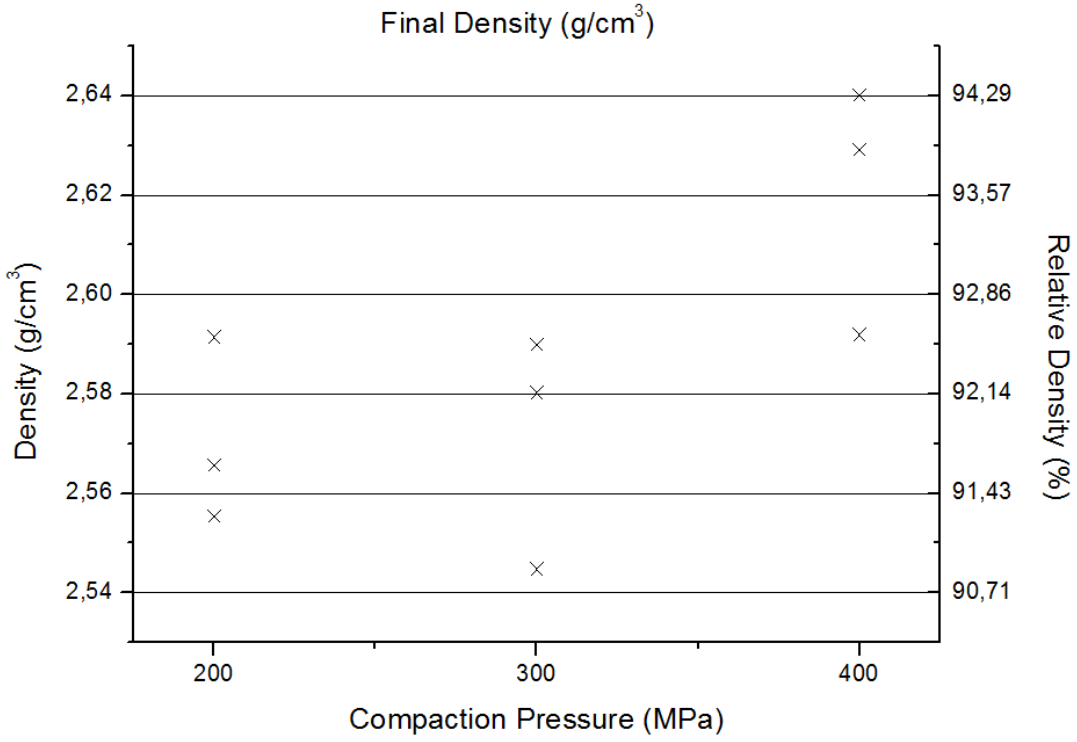

Figure 3.7: Final density.

Table 3.6: Final density.

Compaction Pressure (MPa)	Density (g/cm^3)	Standard Deviation (g/cm^3)	Relative density (%)	Porosity (%)
200	2.57	0.019	91.81	8.19
300	2.57	0.024	91.84	8.16
400	2.62	0.025	93.58	6.42

Table 3.6 and Figure 3.7 contain the results for the sintered density. For 200 MPa, a 91.81% density was obtained. A similar density, 91.84%, was reached for 300 MPa. For 400 MPa, a relative density of 93.58% was achieved, similar to the obtained by previous works [34, 35, 41].

3.3.2. Bending Strength

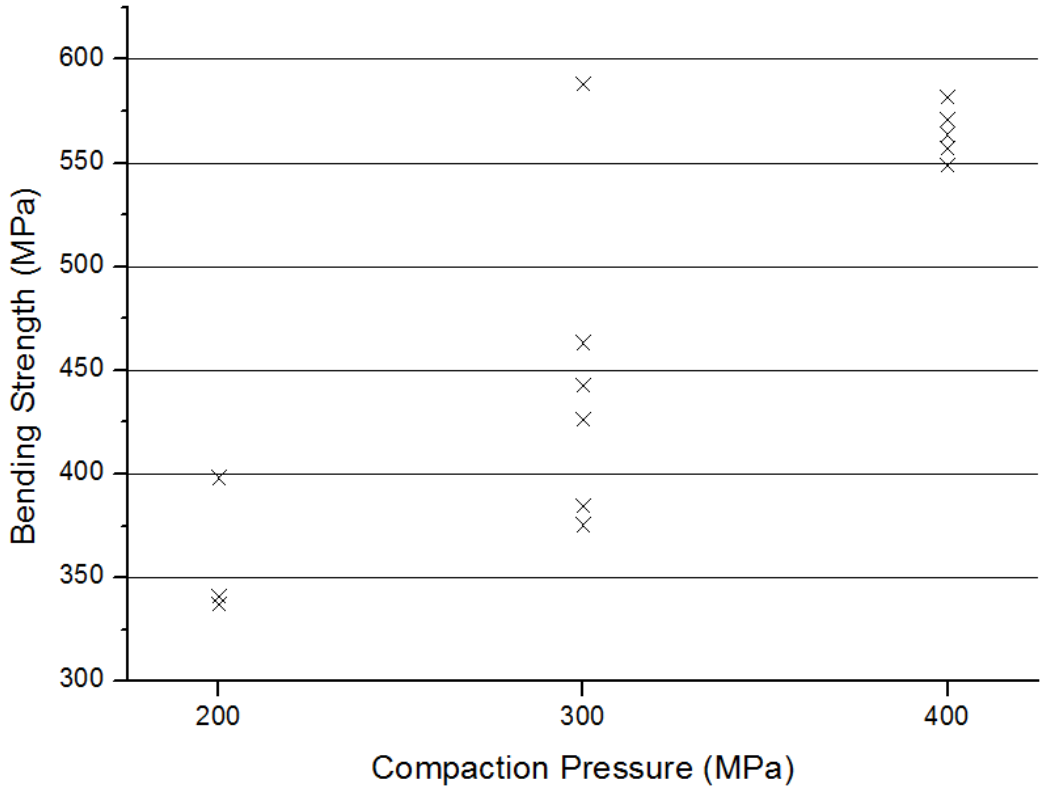

Figure 3.8: Bending Strength of the heat treated samples.

Table 3.7: Average bending strength of the heat treated samples.

Compaction Pressure (MPa)	Bending strength (MPa)	Standard Deviation (MPa)
200	358.83	34.15
300	446.64	76.93
400	564.31	12.64

The bending strength test results can be seen on Figure 3.8 and Table 3.7. Respectively, for 200, 300 and 400 MPa compaction pressure, the average results are 358.83, 446.64 and 564.31 in MPa.

3.3.3. Hardness

For the hardness test, each sintered and heat treated sample was measured six times, with the results being shown in Figure 3.9 and Table 3.8. For comparison, the Vickers Hardness of forged AA2014 T4 is 118 HV [42]. For the samples compacted at 400 MPa, porosity reduces that value in a 25%.

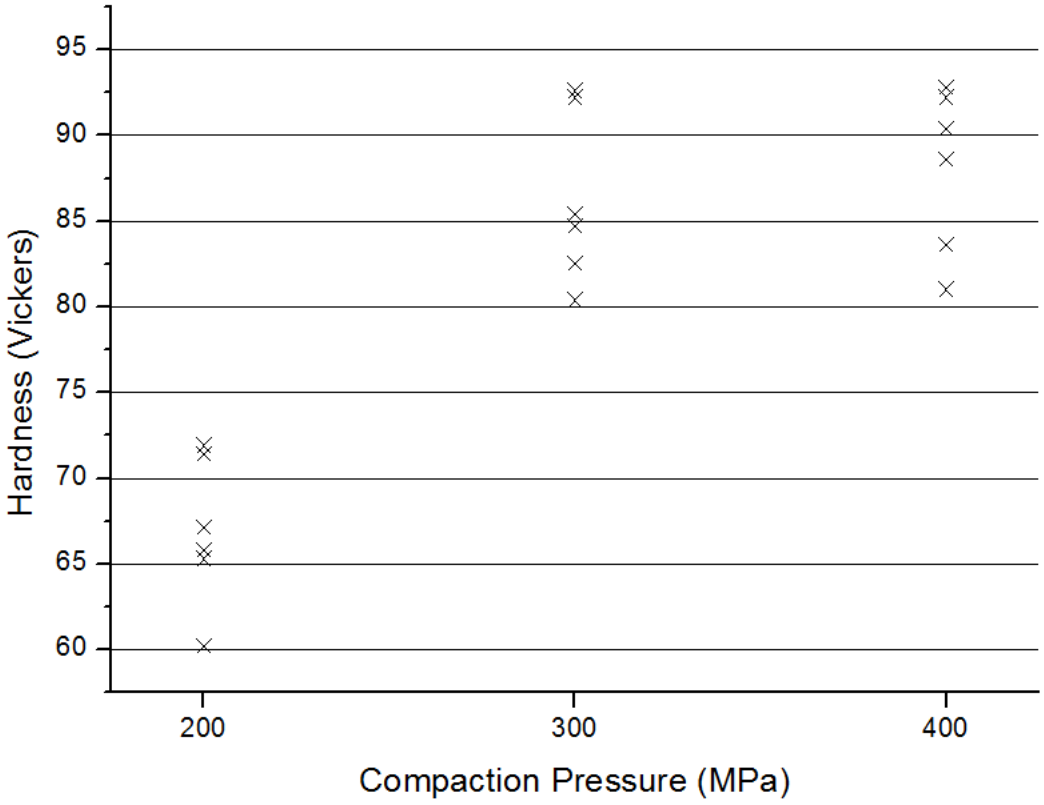

Figure 3.9: Hardness.

Table 3.8: Average hardness.

Compaction Pressure (MPa)	Hardness (HV)	Standard Deviation
200	66.98	4.33
300	86.36	5.04
400	88.10	4.80

3.3.4. Microstructure: SEM and XRD

Scanning Electron Microscopy (SEM)

Figure 3.10 shows images obtained at 500 magnifications. It includes pictures of samples only sintered and samples sintered and heat treated.

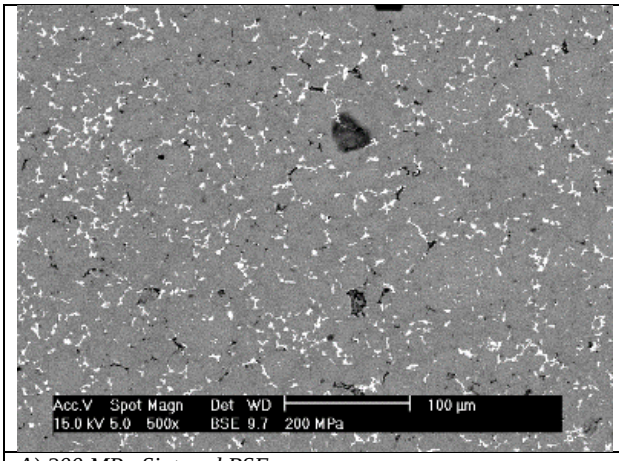

A) 200 MPa Sintered BSE

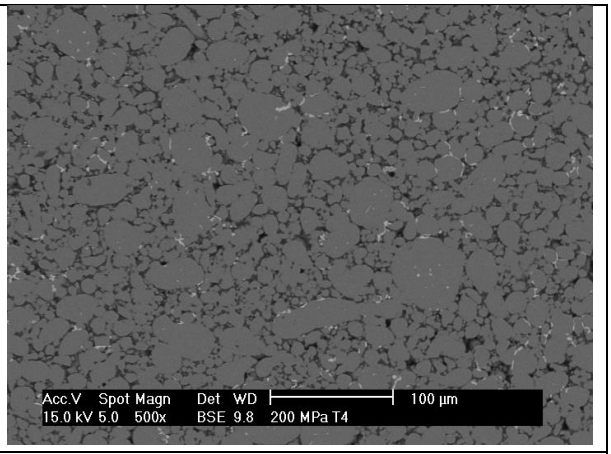

B) 200 MPa T4 BSE

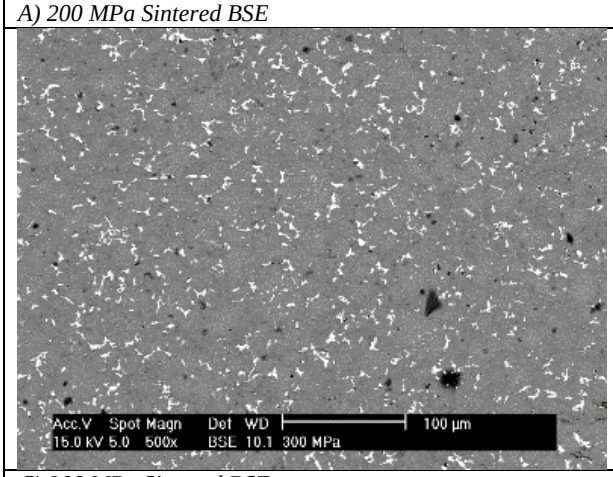

C) 300 MPa Sintered BSE

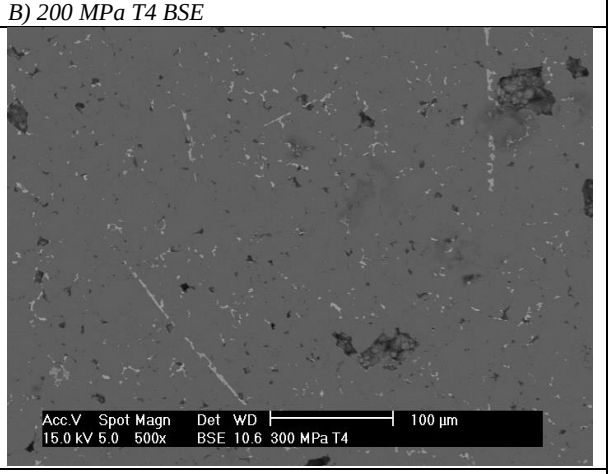

D) 300 MPa T4 BSE

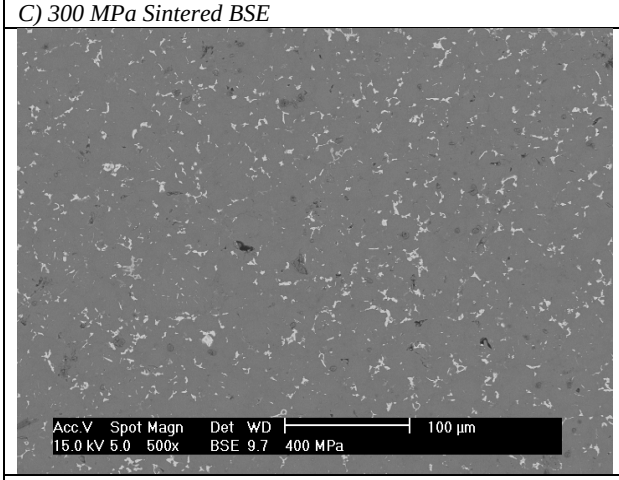

E) 400 MPa Sintered BSE

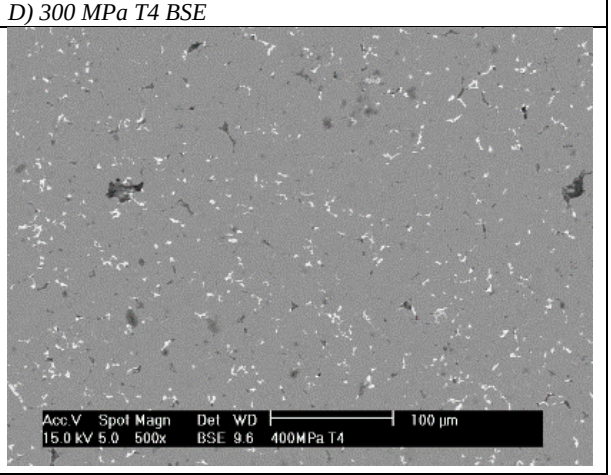

G) 400 MPa T4 BSE

Figure 3.10: SEM microstructures at 500 magnifications.

Figure 3.11 shows images obtained at 2000 magnifications to better appreciate the precipitates differences in shape and color.

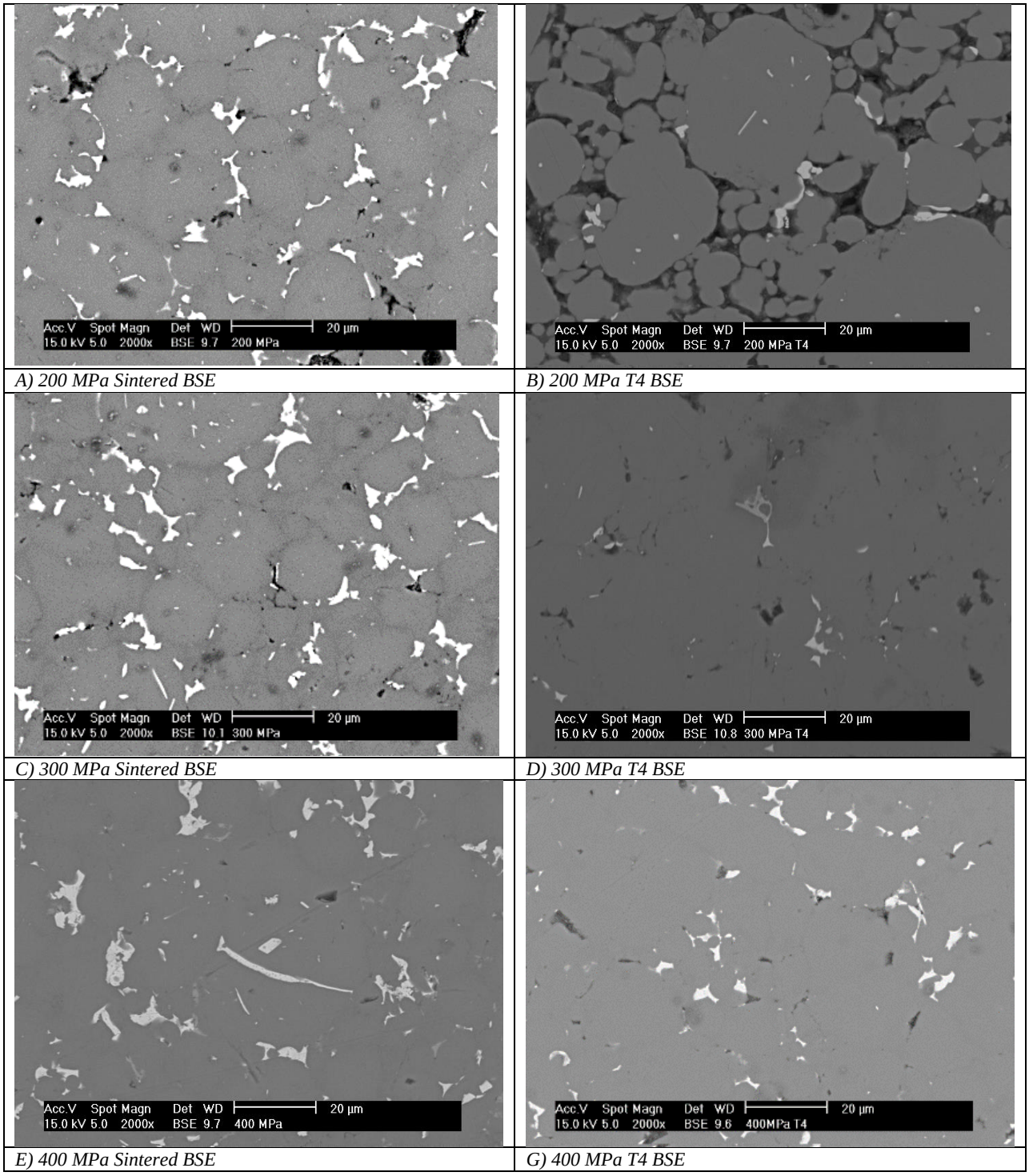

A) 200 MPa Sintered BSE | *B) 200 MPa T4 BSE*

C) 300 MPa Sintered BSE | *D) 300 MPa T4 BSE*

E) 400 MPa Sintered BSE | *G) 400 MPa T4 BSE*

Figure 3.11: SEM microstructures at 2000 magnifications.

First, the porosity can be observed to decrease greatly from 200 MPa to 400 MPa, as expected and as seen in its influence on mechanical properties. In addition, the 200 MPa sample shows problems to fully sinterize.

The grain boundaries can be presumed due to the presence of precipitates, pores, and showing a darker color in general. The grain size can be observed to be similar to the size of the original particles, which had an average of 21.1 µm.

On the left side images, a high number of precipitates can be observed. They are mostly white, of irregular forms and mostly located on the grain boundaries. Analysis with EDX allowed to identify this precipitates as θ-phase, or Al_2Cu (Figure 3.12). On the right side, the samples show

a smaller amount of precipitates, since most of them have been dissolved in the matrix during the heat treatment.

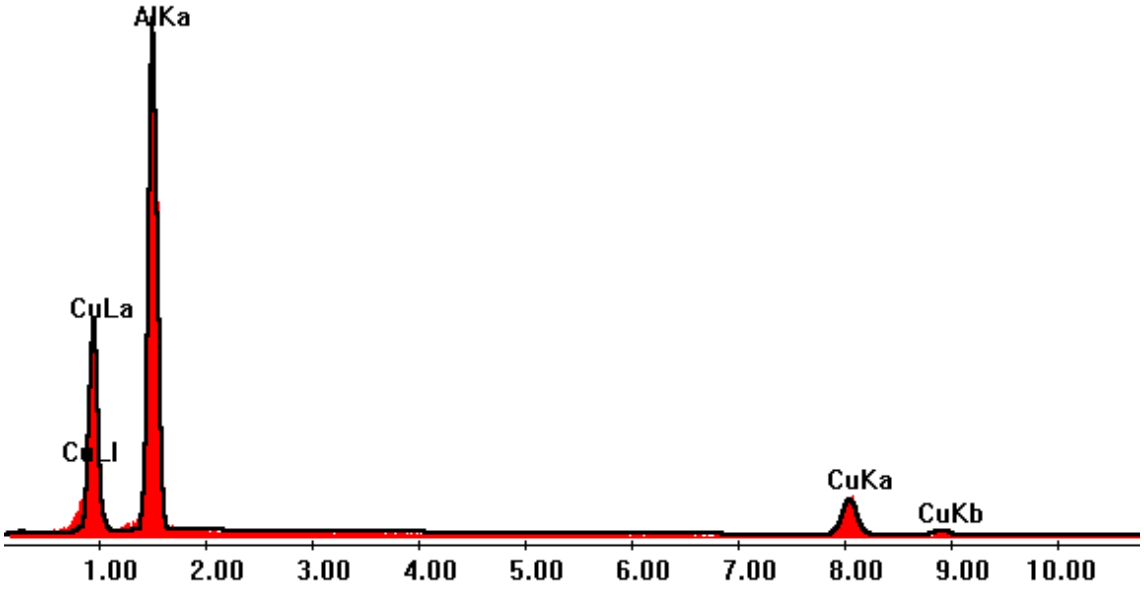

Figure 3.12: EDX of Al2Cu precipitates.

Other precipitates were found in much smaller numbers. Figure 3.13 represent the EDX of an Al-Mg-Si-Cu intermetallic, containing in atomic weight 69.73% Al, 15.02% Si, 12.01% Mg and 3.24% Cu. Another precipitate showed an iron impurity of composition 71.71 % Al, 11.61% Fe, 9.65% Si and smaller amounts of Cu and Mg (Figure 3.14). It could be a mixture of $Al_{12}Fe_3Si$ and other intermetallics, such as Al_7Cu_2Fe or Al_6 (Fe,Cu).

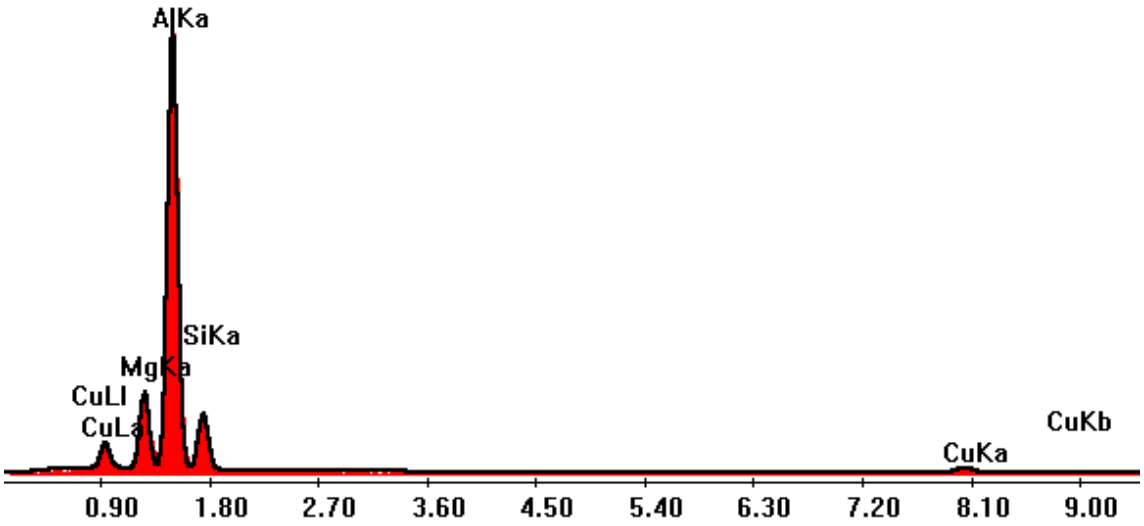

Figure 3.13: Al-Mg-Si-Cu Intermetallic.

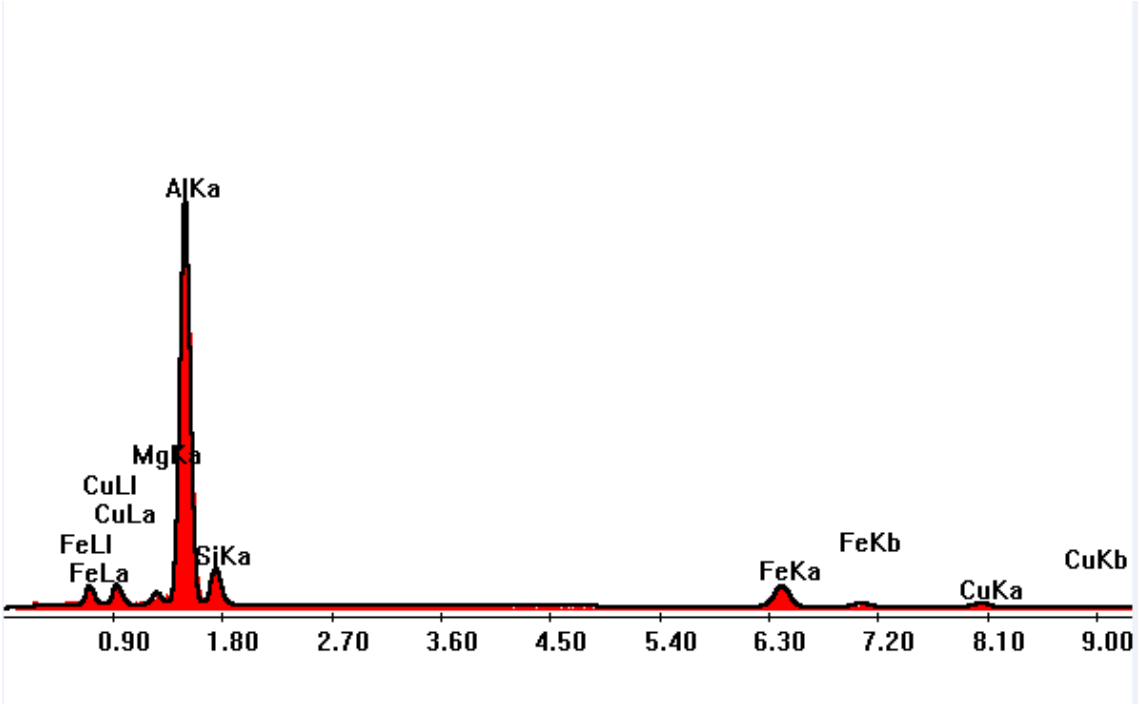

Figure 3.14: Al-Fe-Si.

X Rays Diffraction (XRD)

The XRD of both the sintered, and sintered and heat treated samples are shown in Figures 3.15 and 3.16, respectively. The phases found are again Al-alpha and, in a much smaller proportion, the intermetallic Al_2Cu. In the heat treated samples, the intermetallic is harder to identify, as seen in the SEM images.

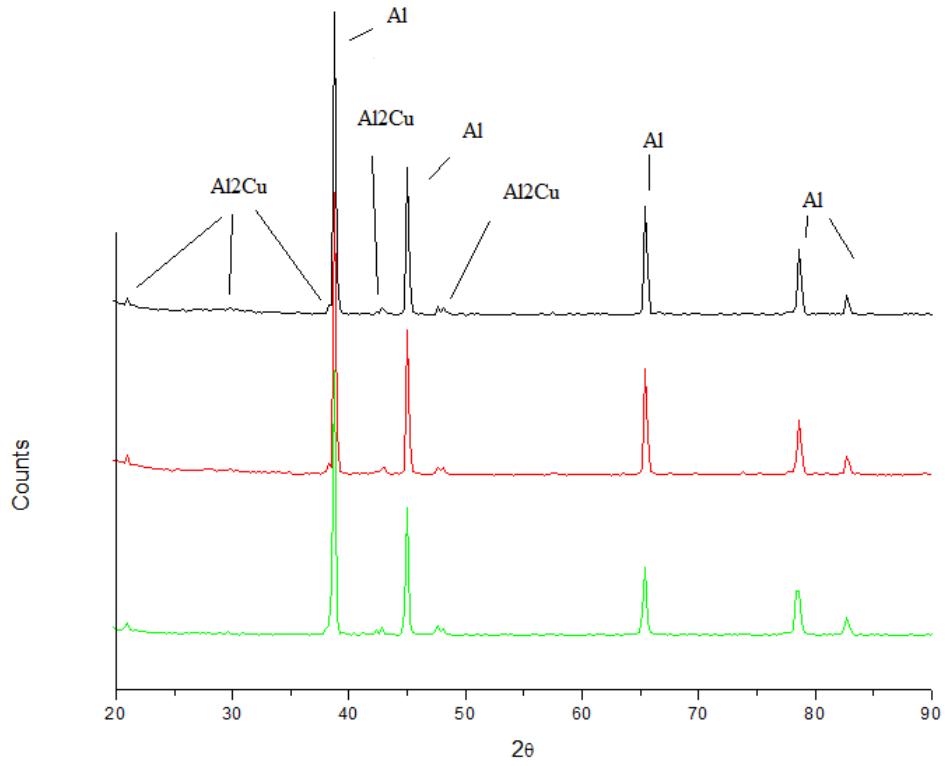

Figure 3.15: XRD analysis of sintered samples at different compaction pressures: 200 MPa (top), 300 MPa (middle) and 400 MPa (bottom).

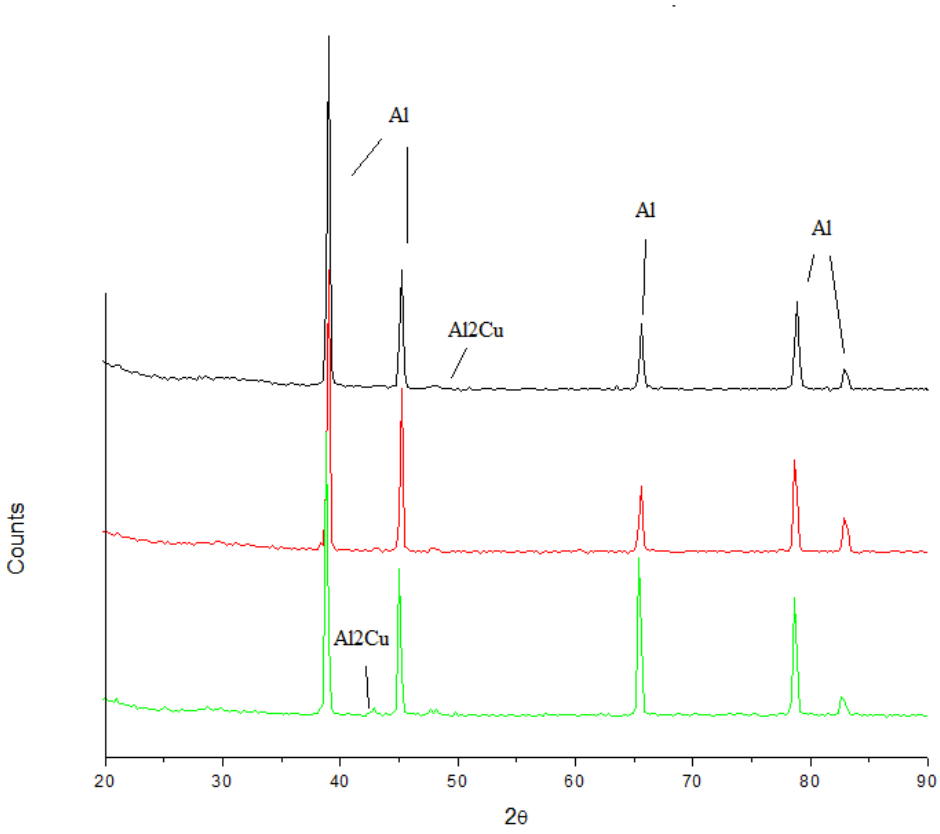

Figure 3.16: XRD analysis of heat treated samples at different compaction pressures: 200 MPa (top), 300 MPa (middle) and 400 MPa (bottom).

3.4. Electrochemical corrosion: Electrochemical Impedance Spectroscopy (EIS)

The equivalent circuit employed is represented in Figure 3.17. R_e is a resistance associated with the electrolyte, $CPEo_{xd}$ and Ro_{xd} represent the resistance and capacity of the pores and defects of the oxide, and R_{polar} and CPE_{dl} take into account the resistance of the polarization and the capacity of the electrochemical double layer, respectively. Each of the impedances were adjusted from 10 KHz to 0.01 Hz.

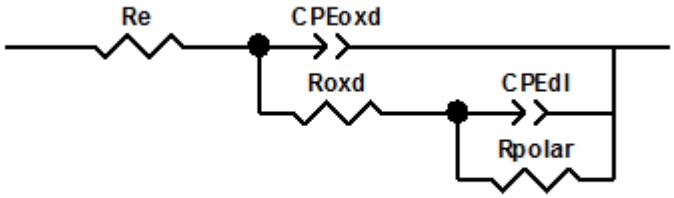

Figure 3.17. Equivalent circuit.

Figures 3.18-20 shows the Nyquist plot and Bode diagrams of the 200, 300 and 400 MPa samples, respectively, after different times of immersion: 2h, 8h, 12h, 18h and 24h. When looking at the phase diagram, two different time constants can be observed at different frequencies. At mid-high frequencies, the time constant indicates the presence of an oxide layer over the matrix while at low frequencies the other time constant at lower frequencies represents the oxidation of the metal.

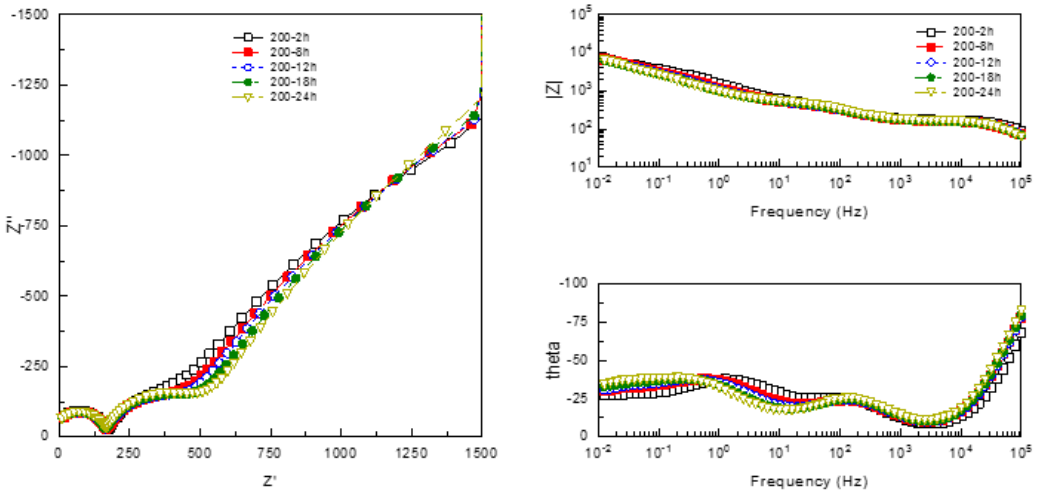

Figure 3.18: Nyquist plot and Bode diagram for the 200 MPa sample, immersed in a Harrison solution for 2h, 8h, 12h, 18h and 24h.

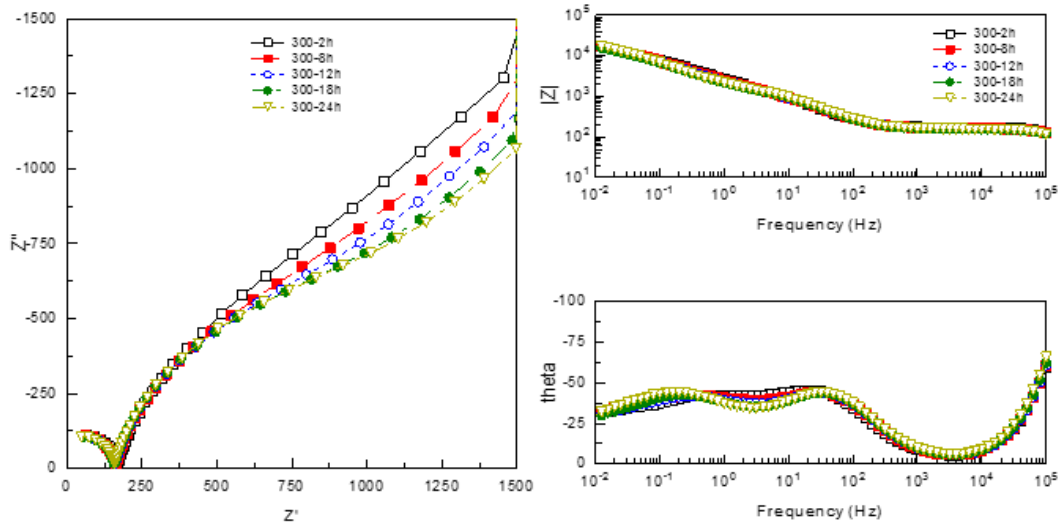

Figure 3.19: Nyquist plot and Bode diagram for the 300 MPa sample, immersed in a Harrison solution for 2h, 8h, 12h, 18h and 24h.

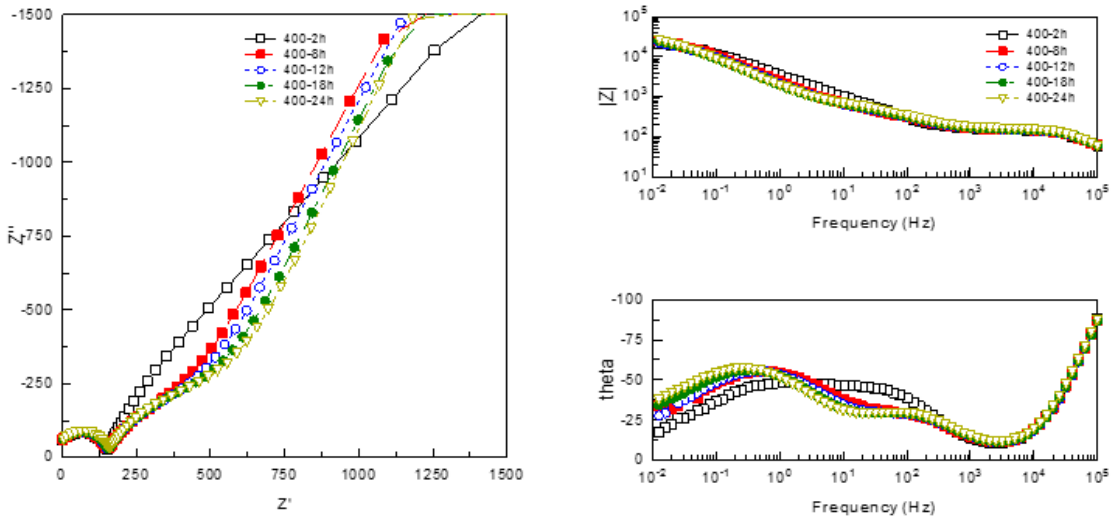

Figure 3.20: Nyquist plot and Bode diagram for the 400 MPa sample, immersed in a Harrison solution for 2h, 8h, 12h, 18h and 24h .

Tables 3.9 and 3.10 show the value of the different elements that form the equivalent circuit, at 2 and 24 hours of immersion, respectively. R_e is similar across all compaction pressures and immersion time, which is due to depending on the distance between the working electrode and the reference electrode.

The increases of CPE_{dl} with the immersion time at every compaction pressure can be caused by acidification or increase of the area of the pits. However, since there is no clear trend on R_{ox} nor R_{polar}, both dependant on the area of the pits, the increase of CPE_{dl} is likely linked to the adsorptions of anions by the oxide film that occurs at low pH [43].

The increase of CPE_{ox} may be caused due to a thinning of the layer oxide, since the capacitance is inversely proportional to the thickness of the oxide, or due to the hydration of the oxide film, which reacts with H_2O to form hydrated aluminium oxide. The hydrated layer, having a higher dielectric constant, would be responsible for increasing CPE_{ox}.

Overall, evaluating the resulting equivalent circuits shows the 200 MPa samples to be of a much lower resistance to corrosion than the others, as can be seen in Figures 3.21 and 3.22. This can be attributed to the higher porosity of the sample, as well as a poorest compaction. In accordance with this, the 400 MPa has the best overall resistance to corrosion, also showing a greater resistance to pitting.

Table 3.9: Value of the elements of the equivalent circuit for the samples immersed in a Harrison solution for 2h.

	Compaction Pressure (MPa)		
Element	**200**	**300**	**400**
Re (Ω)	148.4	151.3	128.3
CPEox (µF)	12.01	25.10	44.59
Rox (Ω)	149.1	804.8	1863
CPEdl (µF)	304.28	156.4	61.86
Rpolar (kΩ)	11.20	41.90	23.56
Chi-squared	$3.42 \cdot 10^{-3}$	$5.56 \cdot 10^{-4}$	$8.55 \cdot 10^{-4}$
Weighted sum of squares	0.359	0.058	0.090

Table 3.10: Value of the elements of the equivalent circuit for the samples immersed in a Harrison solution for 24h.

	Compaction Pressure (MPa)		
Element	**200**	**300**	**400**
Re (Ω)	141.3	141.1	121.8
CPEox (µF)	19.91	25.65	89.41
Rox (Ω)	319.3	1177	959.3
CPEdl (µF)	567.10	204.15	79.91
Rpolar (kΩ)	12.74	27.01	49.27
Chi-squared	$1.52 \cdot 10^{-3}$	$3.31 \cdot 10^{-4}$	$6.20 \cdot 10^{-4}$
Weighted sum of squares	0.160	0.035	0.065

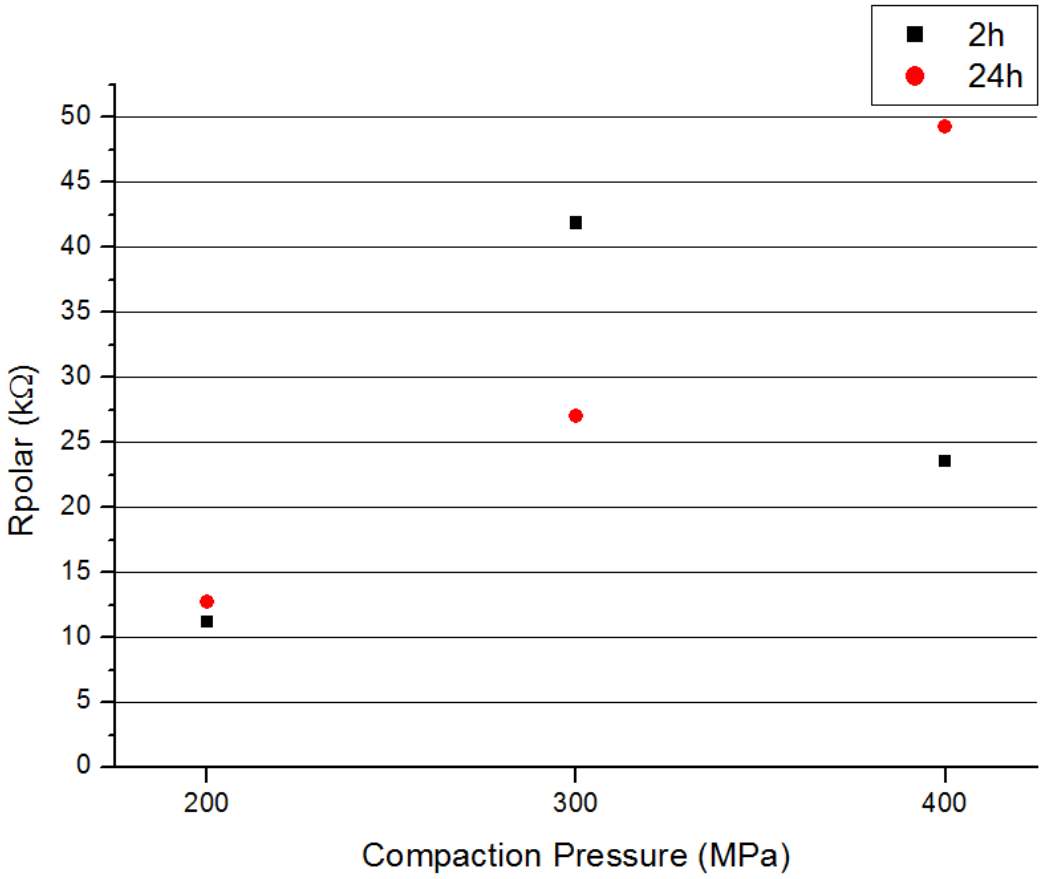

Figure 3.21: Variation of R_{polar} with compaction pressure and thus, porosity, at 2h and 24h of immersion.

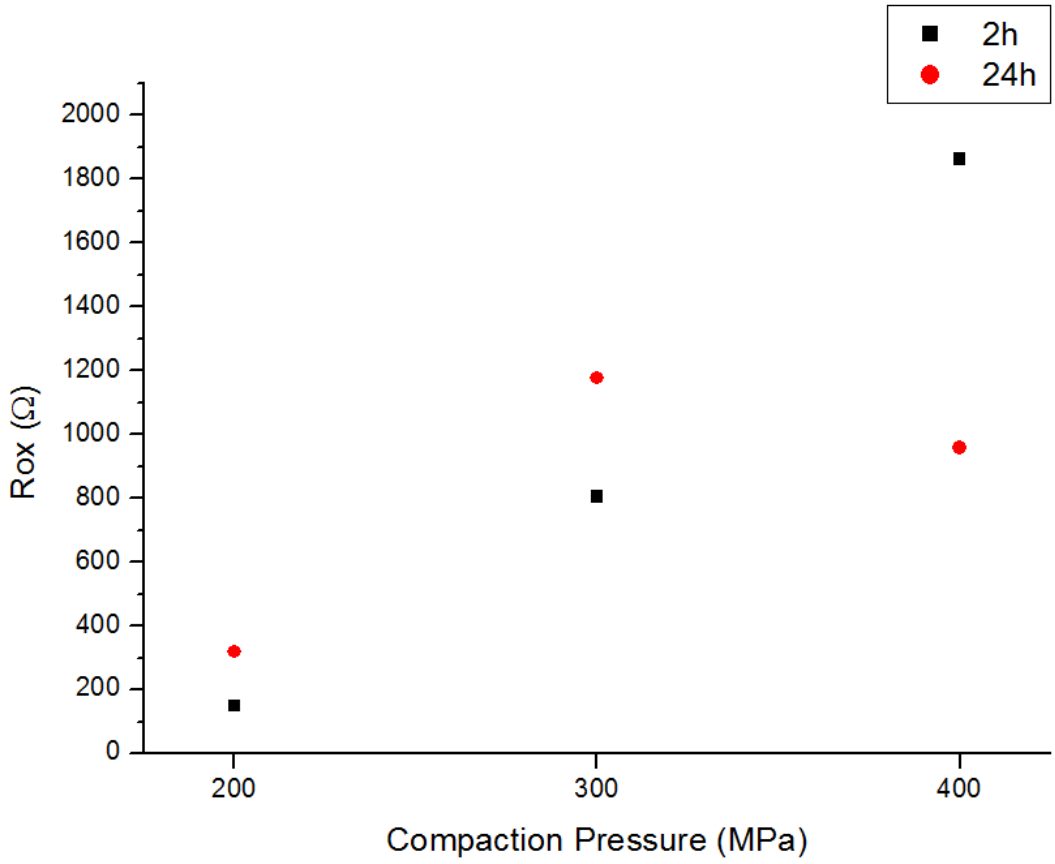

Figure 3.22: Variation of R_{ox} with compaction pressure and thus, porosity, at 2h and 24h of immersion.

CHAPTER 4: CONCLUSIONS

The starting powders where found to be spherical and of an average particle size of 21.1 µm. The characterization of the microstructure showed the presence of the intermetallic Al_2Cu.

The poor compatibility of the powders, caused by the small size and them being pre-alloyed, required 1.5% of Acrawax to be added before compaction.

200 MPa showed to be quite lacking, with some of the samples failing to compact adequately. Compaction pressures over 400 MPa showed delamination of the samples. The 400 MPa samples reached green densities of 84.70% and bending strength of 4.22 MPa.

The theoretical study of the phase diagram showed that a 25% molar fraction would be liquid at the sintering temperature. In addition, the solvus line is at around 510 ºC. The heat treatment temperature of 495 ºC was able to dissolve most of the intermetallics. The themogravimetric analysis showed that the lubricant was being burned between 200 ºC and 400 ºC.

After the sintering and heat treatment, the 400 MPa samples were able to reach 93.58% relative density, a bending strength of 564.31 MPa and a hardness of 88.10 HV. The 300 MPa samples reached 91.84% relative density and similar values of hardness as the 400 MPa samples.

The microstructure characterization, XRD and SEM, showed a reduction of the Al_2Cu intermetallics. In much smaller proportions, other precipitates of the alloyants where found, including some iron impurities. The 200 MPa samples showed a worse sinterization when compared to the other samples.

The electrochemical impedance spectroscopy allowed us to determine the values of the equivalent circuit elements that should accurately explain the corrosion behavior of the material. The 200 MPa showed again to be the worse sample, with overall lower resistance corrosion than the others.

With the obtained results at hand, for the future it is proposed to further study the electrochemical behavior of the material, with the focus on the influence of the precipitates in the corrosion process.

In addition, in order to improve the mechanical properties, future studies could focus on improving the final density of the parts. This could be achieved by modifying sintering conditions, the particle size distribution or the compaction technique, such as using double-action instead of single-action.

CHAPTER 5: REFERENCES

1. Elwin L. Rooy, A.C.o.A., *Introduction to Aluminum and Aluminum Alloys.* **ASM Metals HandBook Volume 02 - Properties and Selection Nonferrous Alloys and Special-Purpose Materials**.
2. Sverdlin, A., *Introduction to Aluminum.* **Handbook of Aluminium Volume 1 - Physical Metallurgy and Processes**.
3. Sverdlin, A., *Properties of Pure Aluminium.* **Handbook of Aluminium Volume 1 - Physical Metallurgy and Processes**.
4. Vargel, C., *Aluminium and Its Alloys.* **Corrosion of Aluminium**.
5. Staley, M.T.a.J.T., *Physical Metallurgy and the Effect of Alloying Additions in Aluminium Alloys.* **Handbook of Aluminium Volume 1 - Physical Metallurgy and Processes**.
6. R.B.C. Cayless, A.R.P.C., *Alloy and Temper Designation Systems for Aluminum and Aluminum Alloys.* **ASM Metals HandBook Volume 02 - Properties and Selection Nonferrous Alloys and Special-Purpose Materials**.
7. Jack W. Bray, R.M.C., *Aluminum Mill and Engineered Wrought Products.* **ASM Metals HandBook Volume 02 - Properties and Selection Nonferrous Alloys and Special-Purpose Materials**.
8. *Properties of Wrought Aluminum and Aluminum Alloys.* **ASM Metals HandBook Volume 02 - Properties and Selection Nonferrous Alloys and Special-Purpose Materials**.
9. Charlie R. Brooks, U.o.T., *Principles of Heat Treating of Nonferrous Alloys.* **ASM Metals Handbook Volume 04 - Heat Treating**.
10. Laurens Katgerman and D. Eskin, N.I.f.M.R., Delft, The Netherlands, *Hardening, Annealing, and Aging.* **Handbook of aluminium - Volumen 1 Physical metallurgy and processes**.
11. White, D.G., *History of Powder Metallurgy.* **ASM Metals HandBook Volume 07 - Powder Metal Technologies and Applications**.
12. Sanderow, H.I., *Powder Metallurgy Methods and Design.* **ASM Metals HandBook Volume 07 - Powder Metal Technologies and Applications**.
13. B. Lynn Ferguson, D.C.T., Inc.; Randall M. German, The Pennsylvania State University, *Powder Shaping and Consolidation Technologies.* **ASM Metals HandBook Volume 07 - Powder Metal Technologies and Applications**.
14. Revised by John Porter, C.I., *Powder Metallurgy Presses and Tooling.* **ASM Metals HandBook Volume 07 - Powder Metal Technologies and Applications**.
15. Revised by Randall M. German, P.S.U., *Consolidation Principles and Process Modeling.* **ASM Metals HandBook Volume 07 - Powder Metal Technologies and Applications**.
16. *Production Sintering Practices.* **ASM Metals HandBook Volume 07 - Powder Metal Technologies and Applications**.
17. *Conventional Aluminum Powder Metallurgy Alloys.* **ASM Metals HandBook Volume 07 - Powder Metal Technologies and Applications**.
18. Tim Raffeinner, A.F.C.H.S.N., BOC Gas Inc., *Sintering Furnaces and Atmospheres.* **ASM Metals HandBook Volume 07 - Powder Metal Technologies and Applications**.
19. Rajiv Tandon, P.P.M.M.J.J., Howmet Corporation, *Liquid-Phase Sintering.* **ASM Metals HandBook Volume 07 - Powder Metal Technologies and Applications**.
20. Vargel, C., *The Corrosion of Aluminium.* **Corrosion of Aluminium**.
21. Miroslav I. Marek, S.o.M.E., Georgia Institute of Technology, *Fundamentals of Corrosion - Introduction.* **ASM Metals Handbook Volume 13 - Corrosion**.
22. E.H. Hollingsworth (retired) and H.Y. Hunsicker (retired), A.C.o.A., *Corrosion of Aluminum and Aluminum Alloys.* **ASM Metals Handbook Volume 13 - Corrosion**.
23. *Corrosion in the Aircraft Industry.* **ASM Metals Handbook Volume 13 - Corrosion**.

24. A.I. Asphahani and W.L. Silence, H.I., Inc., *Localized Corrosion - Pitting Corrosion.* **ASM Metals Handbook Volume 13 - Corrosion**.
25. G.S. Frankel, T.O.S.U., *Pitting Corrosion.* **Asm Metals Handbook Volume 13A - Corrosion Fundamentals, Testing, And Protection**.
26. Szklarska-Smialowska, Z., *Pitting corrosion of aluminum.*
27. N. Birbilis*, a.R.G.B., *Electrochemical Characteristics of Intermetallic Phases in Aluminum Alloys.*
28. A. Boag, A.E.H., A.M. Glenn, T.H. Muster, D. McCulloch, *Corrosion of AA2024-T3 Part I: Localised corrosion of isolated IM particles.*
29. Antonia Jiménez-Morales, J.C.G.S., *ESPECTROSCOPÍA DE IMPEDANCIA ELECTROQUÍMICA APLICADA AL ESTUDIO DE LA CORROSIÓN Y PROTECCIÓN DE SUPERFICIES METÁLICAS.*
30. C. D. Boland and D. P. Bishop, D.U., R.L. Hexemer jr. and I.W. Donaldson, GKN Sinter Metals LLC, *On the Development of an Aluminum PM Alloy for "Press-Sinter-Size" Technology.*
31. C.D. Boland, R.L.H.J., I.W. Donaldsonb,D.P. Bishop, *Industrial processing of a novel Al–Cu–Mg powder metallurgy alloy.*
32. 2738:2000, I., *Sintered metal materials, excluding hardmetals. Permeable sintered metal materials. Determination of density, oil content and open porosity*
33. 3325/A1:2002, U.-E.I., *Sintered metal materials, excluding hardmetals - Determination of transverse rupture strength - Amendment 1: Precision statement. (ISO 3325:1996/Amd. 1:2001).*
34. G.B. Schaffer, T.B.S., R.N. Lumley, *Liquid phase sintering of aluminium alloys.*
35. J.M. Martín, F.C., *Liquid phase sintering of P/M aluminium alloys: effect of processing conditions.*
36. M. Yan, P.Y., G.B. Schaffer, M. Qian, *Secondary phases and interfaces in a nitrogen-atmosphere sintered Al alloy: Transmission electron microscopy evidence for the formation of AlN during liquid phase sintering.*
37. G.B. Schaffer, J.-Y.Y., S.J. Bonner, E. Crossin, S.J. Pas, A.J. Hill, *The effect of tin and nitrogen on liquid phase sintering of Al–Cu–Mg–Si alloys.*
38. 6507-1:2005, I., *Metallic materials -- Vickers hardness test --.*
39. Ram B. Bhagat, T.P.S.U., *Advanced Aluminum Powder Metallurgy Alloys and Composites.* **ASM Metals HandBook Volume 07 - Powder Metal Technologies and Applications**.
40. P. Beiss, K.D., R. Peters, *Aluminium Powders.* **International Atlas of Powder Metallurgical Microstructures**.
41. Azim Gökçe, F.F., Ali Osman Kurt, *Microstructural examination and properties of premixed Al–Cu–Mg powder metallurgy alloy.*
42. Inc., A.A.S.M. *Aluminum 2014-T4; 2014-T451 ASM Datasheet*. 2014 7/9/2014]; Available from: http://asm.matweb.com/search/SpecificMaterial.asp?bassnum=MA2014T4.
43. J.A. Moreto, C.E.B.M., W.W. Bose Filho, L.A. Rocha, J.C.S. Fernandes, *SVET, SKP and EIS study of the corrosion behaviour of high strength Al and Al–Li alloys used in aircraft fabrication.*